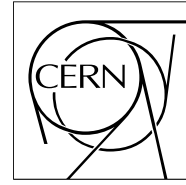


The Compact Muon Solenoid Experiment

CMS Note

Mailing address: CMS CERN, CH-1211 GENEVA 23, Switzerland



18 March 2008

Performance studies of the CMS Strip Tracker before installation

W. Adam, T. Bergauer, M. Dragicevic, M. Friedl, R. Frühwirth, S. Häsnel, J. Hrubec, M. Krammer, M. Oberegger,
M. Pernicka, S. Schmid, R. Stark, H. Steininger, D. Uhl, W. Waltenberger, E. Widl

Institut für Hochenergiephysik der Österreichischen Akademie der Wissenschaften (HEPHY), Vienna, Austria

P. Van Mechelen, M. Cardaci, W. Beaumont, E. de Langhe, E. A. de Wolf, E. Delmeire

Universiteit Antwerpen, Belgium

O. Bouhali, O. Charaf, B. Clerbaux, J.-P. Dewulf, S. Elgammal, G. Hammad, G. de Lentdecker, P. Marage,
C. Vander Velde, P. Vanlaer, J. Wickens

Université Libre de Bruxelles, ULB, Bruxelles, Belgium

V. Adler, O. Devroede, S. De Weirtdt, J. D'Hondt, R. Goorens, J. Heyninck, J. Maes, M. Mozer, S. Tavernier,
L. Van Lancker, P. Van Mulders, I. Villella, C. Wastiels

Vrije Universiteit Brussel, VUB, Brussel, Belgium

J.-L. Bonnet, G. Bruno, B. De Callatay, B. Florins, A. Giammanco, G. Gregoire, Th. Keutgen, D. Kcira,
V. Lemaitre, D. Michotte, O. Militaru, K. Piotrkowski, L. Quertermont, V. Roberfroid, X. Rouby, D. Teyssier, M.
Vander Donckt

Université catholique de Louvain, UCL, Louvain-la-Neuve, Belgium

E. Daubie

Université de Mons-Hainaut, Mons, Belgium

E. Anttila, S. Czellar, P. Engström, J. Härkönen, V. Karimäki, J. Kortesmaa, A. Kuronen, T. Lampén, T. Lindén,
P. -R. Luukka, T. Mäenpää, S. Michal, E. Tuominen, J. Tuominiemi

Helsinki Institute of Physics, Helsinki, Finland

M. Ageron, G. Baulieu, A. Bonnevaux, G. Boudoul, E. Chabanat, E. Chabert, R. Chierici, D. Contardo, R. Della
Negra, T. Dupasquier, G. Gelin, N. Giraud, G. Guillot, N. Estre, R. Haroutunian, N. Lumb, S. Perries, F. Schirra,
B. Trocme, S. Vanzetto

Université de Lyon, Université Claude Bernard Lyon 1, CNRS/IN2P3, Institut de Physique Nucléaire de Lyon, France

J.-L. Agram, R. Blaes, F. Drouhin^{a)}, J.-P. Ernenwein, J.-C. Fontaine

Groupe de Recherches en Physique des Hautes Energies, Université de Haute Alsace, Mulhouse, France

J.-D. Berst, J.-M. Brom, F. Didierjean, U. Goerlach, P. Graehling, L. Gross, J. Hosselet, P. Juillot, A. Lounis,
C. Maazouzi, C. Olivetto, R. Strub, P. Van Hove

Institut Pluridisciplinaire Hubert Curien, Université Louis Pasteur Strasbourg, IN2P3-CNRS, France

G. Anagnostou, R. Brauer, H. Esser, L. Feld, W. Karpinski, K. Klein, C. Kukulies, J. Olzem, A. Ostapchuk,
D. Pandoulas, G. Pierschel, F. Raupach, S. Schael, G. Schwering, D. Sprenger, M. Thomas, M. Weber,
B. Wittmer, M. Wlochal

I. Physikalisches Institut, RWTH Aachen University, Germany

F. Beissel, E. Bock, G. Flugge, C. Gillissen, T. Hermanns, D. Heydhausen, D. Jahn, G. Kaussen^{b)}, A. Linn,
L. Perchalla, M. Poettgens, O. Pooth, A. Stahl, M. H. Zoeller

III. Physikalisches Institut, RWTH Aachen University, Germany

P. Buhmann, E. Butz, G. Flucke, R. Hamdorf, J. Hauk, R. Klanner, U. Pein, P. Schleper, G. Steinbrück

University of Hamburg, Institute for Experimental Physics, Hamburg, Germany

P. Blüm, W. De Boer, A. Dierlamm, G. Dirkes, M. Fahrner, M. Frey, A. Furgeri, F. Hartmann^{a)}, S. Heier,
K.-H. Hoffmann, J. Kaminski, B. Ledermann, T. Liamsuwan, S. Müller, Th. Müller, F.-P. Schilling,
H.-J. Simonis, P. Steck, V. Zhukov

Karlsruhe-IEKP, Germany

P. Cariola, G. De Robertis, R. Ferorelli, L. Fiore, M. Preda,^{c)} G. Sala, L. Silvestris, P. Tempesta, G. Zito

INFN Bari, Italy

D. Creanza, N. De Filippis^{d)}, M. De Palma, D. Giordano, G. Maggi, N. Manna, S. My, G. Selvaggi

INFN and Dipartimento Interateneo di Fisica, Bari, Italy

S. Albergo, M. Chiorboli, S. Costa, M. Galanti, N. Giudice, N. Guardone, F. Noto, R. Potenza, M. A. Saizu^{c)},
V. Sparti, C. Sutera, A. Tricomi, C. Tuvè

INFN and University of Catania, Italy

M. Brianzi, C. Civinini, F. Maletta, F. Manolescu, M. Meschini, S. Paoletti, G. Sguazzoni

INFN Firenze, Italy

B. Broccolo, V. Ciulli, R. D'Alessandro, E. Focardi, S. Frosali, C. Genta, G. Landi, P. Lenzi, A. Macchiolo,
N. Magini, G. Parrini, E. Scarlini

INFN and University of Firenze, Italy

G. Cerati

INFN and Università degli Studi di Milano-Bicocca, Italy

P. Azzi, N. Bacchetta^{a)}, A. Candelori, T. Dorigo, A. Kaminsky, S. Karaevski, V. Khomenkov^{b)}, S. Reznikov,
M. Tessaro

INFN Padova, Italy

D. Bisello, M. De Mattia, P. Giubilato, M. Loreti, S. Mattiazzo, M. Nigro, A. Paccagnella, D. Pantano,
N. Pozzobon, M. Tosi

INFN and University of Padova, Italy

G. M. Bilei^{a)}, B. Checcucci, L. Fanò, L. Servoli

INFN Perugia, Italy

F. Ambroglini, E. Babucci, D. Benedetti^{e)}, M. Biasini, B. Caponeri, R. Covarelli, M. Giorgi, P. Lariccia,
G. Mantovani, M. Marcantonini, V. Postolache, A. Santocchia, D. Spiga

INFN and University of Perugia, Italy

G. Bagliesi, G. Balestri, L. Berretta, S. Bianucci, T. Boccali, F. Bosi, F. Bracci, R. Castaldi, M. Ceccanti, R. Cecchi, C. Cerri, A. S. Cucoanes, R. Dell'Orso, D. Dobur, S. Dutta, A. Giassi, S. Giusti, D. Kartashov, A. Kraan, T. Lomtadze, G. A. Lungu, G. Magazzù, P. Mammini, F. Mariani, G. Martinelli, A. Moggi, F. Palla, F. Palmonari, G. Petragnani, A. Profeti, F. Raffaelli, D. Rizzi, G. Sanguinetti, S. Sarkar, D. Sentenac, A. T. Serban, A. Slav, A. Soldani, P. Spagnolo, R. Tenchini, S. Tolaini, A. Venturi, P. G. Verdini^{a)}, M. Vos^{f)}, L. Zaccarelli

INFN Pisa, Italy

C. Avanzini, A. Basti, L. Benucci^{g)}, A. Bocci, U. Cazzola, F. Fiori, S. Linari, M. Massa, A. Messineo, G. Segneri, G. Tonelli

University of Pisa and INFN Pisa, Italy

P. Azzurri, J. Bernardini, L. Borrello, F. Calzolari, L. Foà, S. Gennai, F. Ligabue, G. Petrucciani, A. Rizzi^{h)}, Z. Yangⁱ⁾

Scuola Normale Superiore di Pisa and INFN Pisa, Italy

F. Benotto, N. Demaria, F. Dumitrache, R. Farano

INFN Torino, Italy

M.A. Borgia, R. Castello, M. Costa, E. Migliore, A. Romero

INFN and University of Torino, Italy

D. Abbaneo, M. Abbas, I. Ahmed, I. Akhtar, E. Albert, C. Bloch, H. Breuker, S. Butt, O. Buchmüller^{j)}, A. Cattai, C. Delaere^{k)}, M. Delattre, L. M. Edera, P. Engstrom, M. Eppard, M. Gateau, K. Gill, A.-S. Giolo-Nicollerat, R. Grabit, A. Honma, M. Huhtinen, K. Kloukinas, J. Kortessmaa, L. J. Kottelat, A. Kuronen, N. Leonardo, C. Ljuslin, M. Mannelli, L. Masetti, A. Marchioro, S. Mersi, S. Michal, L. Mirabito, J. Muffat-Joly, A. Onnela, C. Paillard, I. Pal, J. F. Pernot, P. Petagna, P. Petit, C. Piccut, M. Pioppi, H. Postema, R. Ranieri, D. Ricci, G. Rolandi, F. Ronga^{l)}, C. Sigaud, A. Syed, P. Siegrist, P. Tropea, J. Troska, A. Tsiros, M. Vander Donckt, F. Vasey

European Organization for Nuclear Research (CERN), Geneva, Switzerland

E. Alagoz, C. Amsler, V. Chiochia, C. Regenfus, P. Robmann, J. Rochet, T. Rommerskirchen, A. Schmidt, S. Steiner, L. Wilke

University of Zürich, Switzerland

I. Church, J. Cole^{m)}, J. Coughlan, A. Gay, S. Taghavi, I. Tomalin

STFC, Rutherford Appleton Laboratory, Chilton, Didcot, United Kingdom

R. Bainbridge, N. Cripps, J. Fulcher, G. Hall, M. Noy, M. Pesaresi, V. Radicciⁿ⁾, D. M. Raymond, P. Sharp^{a)}, M. Stoye, M. Wingham, O. Zorba

Imperial College, London, United Kingdom

I. Goitom, P. R. Hobson, I. Reid, L. Teodorescu

Brunel University, Uxbridge, United Kingdom

G. Hanson, G.-Y. Jeng, H. Liu, G. Pasztor^{o)}, A. Satpathy, R. Stringer

University of California, Riverside, California, USA

B. Mangano

University of California, San Diego, California, USA

K. Affolder, T. Affolder^{p)}, A. Allen, D. Barge, S. Burke, D. Callahan, C. Campagnari, A. Crook, M. D'Alfonso, J. Dietch, J. Garberson, D. Hale, H. Incandela, J. Incandela, S. Jaditz^{q)}, P. Kalavase, S. Kreyer, S. Kyre, J. Lamb, C. Mc Guinness^{r)}, C. Mills^{s)}, H. Nguyen, M. Nikolic^{m)}, S. Lowette, F. Rebassoo, J. Ribnik, J. Richman,

N. Rubinstein, S. Sanhueza, Y. Shah, L. Simms^{r)}, D. Staszak^{t)}, J. Stoner, D. Stuart, S. Swain, J.-R. Vlimant,
D. White

University of California, Santa Barbara, California, USA

K. A. Ulmer, S. R. Wagner

University of Colorado, Boulder, Colorado, USA

L. Bagby, P. C. Bhat, K. Burkett, S. Cihangir, O. Gutsche, H. Jensen, M. Johnson, N. Luzhetskiy, D. Mason,
T. Miao, S. Moccia, C. Noeding, A. Ronzhin, E. Skup, W. J. Spalding, L. Spiegel, S. Tkaczyk, F. Yumiceva,
A. Zatserklyaniy, E. Zerev

Fermi National Accelerator Laboratory (FNAL), Batavia, Illinois, USA

I. Anghel, V. E. Bazterra, C. E. Gerber, S. Khalatian, E. Shabalina

University of Illinois, Chicago, Illinois, USA

P. Baringer, A. Bean, J. Chen, C. Hinchey, C. Martin, T. Moulik, R. Robinson

University of Kansas, Lawrence, Kansas, USA

A. V. Gritsan, C. K. Lae, N. V. Tran

Johns Hopkins University, Baltimore, Maryland, USA

P. Everaerts, K. A. Hahn, P. Harris, S. Nahn, M. Rudolph, K. Sung

Massachusetts Institute of Technology, Cambridge, Massachusetts, USA

B. Betchart, R. Demina, Y. Gotra, S. Korjenevski, D. Miner, D. Orbaker

University of Rochester, New York, USA

L. Christofek, R. Hooper, G. Landsberg, D. Nguyen, M. Narain, T. Speer, K. V. Tsang

Brown University, Providence, Rhode Island, USA

-
- a) Also at CERN, European Organization for Nuclear Research, Geneva, Switzerland
b) Now at University of Hamburg, Institute for Experimental Physics, Hamburg, Germany
c) On leave from IFIN-HH, Bucharest, Romania
d) Now at LLR-Ecole Polytechnique, France
e) Now at Northeastern University, Boston, USA
f) Now at IFIC, Centro mixto U. Valencia/CSIC, Valencia, Spain
g) Now at Universiteit Antwerpen, Antwerpen, Belgium
h) Now at ETH Zurich, Zurich, Switzerland
i) Also Peking University, China
j) Now at Imperial College, London, UK
k) Now at Université catholique de Louvain, UCL, Louvain-la-Neuve, Belgium
l) Now at Eidgenössische Technische Hochschule, Zürich, Switzerland
m) Now at University of California, Davis, California, USA
n) Now at Kansas University, USA
o) Also at Research Institute for Particle and Nuclear Physics, Budapest, Hungary
p) Now at University of Liverpool, UK
q) Now at Massachusetts Institute of Technology, Cambridge, Massachusetts, USA
r) Now at Stanford University, Stanford, California, USA
s) Now at Harvard University, Cambridge, Massachusetts, USA

Abstract

In March 2007 the assembly of the Silicon Strip Tracker was completed at the Tracker Integration Facility at CERN. Nearly 15% of the detector was instrumented using cables, fiber optics, power supplies, and electronics intended for the operation at the LHC. A local chiller was used to circulate the coolant for low temperature operation. In order to understand the efficiency and alignment of the strip tracker modules, a cosmic ray trigger was implemented. From March through July 4.5 million triggers were recorded. This period, referred to as the Sector Test, provided practical experience with the operation of the Tracker, especially safety, data acquisition, power, and cooling systems. This paper describes the performance of the strip system during the Sector Test, which consisted of five distinct periods defined by the coolant temperature. Significant emphasis is placed on comparisons between the data and results from Monte Carlo studies.

^{t)} Now at University of California, Los Angeles, California, USA

Contents

1	Introduction	4
2	Sector Test description	4
2.1	The Tracker Safety and Control Systems	5
2.2	Cosmic Muon Trigger	6
3	Data sets and reconstruction	8
3.1	Reconstruction	8
3.2	Data Quality Monitoring	9
3.3	Data Processing	9
4	Detector Performance based on Calibration Data	10
4.1	Electronic Gain Measurements	11
4.2	Noise Performance Studies	13
4.3	Detector quality	16
5	Detector Performance based on Cosmic Ray Data	17
5.1	Latency Scan	19
5.2	The signal-to-noise	20
5.3	Signal calibration	23
5.4	Validation of Online Zero Suppression	25
5.5	Hit Occupancy	25
5.6	Hit Reconstruction Efficiency	27
6	Simulation	27
7	Simulation Tuning	28
7.1	Signal and Noise	29
7.2	Capacitive Coupling	30
7.3	Cluster width studies	31
8	Conclusions	34

1 Introduction

The CMS Tracker [1] is the inner tracking detector built for the CMS experiment at the CERN Large Hadron Collider. It is a unique instrument in both size and complexity: it contains two systems based on silicon sensor technology, one employing pixels and another using silicon microstrips. The Pixel Detector, which surrounds the beam pipe, consists of three barrel layers and four disk detectors, two on each side of the barrel. It contains 64 million detector channels. The Silicon Strip Tracker, the subject of this paper, surrounds the pixel system and consists of four major subsystems: the Inner Barrel (TIB), Inner Disks (TID), an Outer Barrel (TOB) and two End Caps (TEC). It is the largest silicon detector ever built, with almost 10 million sensor channels covering a surface area of over 200 m². The Silicon Strip Tracker (referred to simply as the Tracker in this note) was designed to measure charged particles with high efficiency and spatial resolution over wide range of momenta, and to operate with minimal intervention for the nominal LHC lifetime of 10 years. Consequently, the quality of the construction, and the performance of the components contained within it, are of vital importance and must be thoroughly evaluated under realistic conditions before operation at LHC.

First experience of the operation and detector performance of the Tracker was gained during summer 2006, with a small fraction (1%) of the detector inserted in the CMS experiment. Cosmic rays were detected in the presence of a 4 T solenoidal field and all the CMS sub-detectors were read out. The results are summarized in Ref. [2].

Silicon Strip Tracker construction proceeded during 2006 and 2007: a brief account of the integration and assembly processes can also be found in [3]; it was an endeavour shared by the entire Tracker collaboration and tasks were distributed throughout much of the world. The final assembly of the Tracker was carried out in a large, purpose-built, clean area at CERN: the Tracker Integration Facility (TIF). This facility was instrumented with a significant fraction of the final infrastructure and services needed to operate, control and read out a sector of the Tracker that corresponds to 15% of the entire detector: cables, patch panels, optical fibers, cooling manifolds and rack mounted power supplies and off-detector electronics were installed to allow connection to data acquisition; cooling, control and safety systems were implemented; a trigger system was devised to detect cosmic rays traversing the Tracker, and dedicated computing resources were provided.

Following assembly of the sub-system and prior to the installation into CMS, the detector was commissioned and operated for several months at the TIF, a period referred to as the Sector Test. The goals of this test included commissioning the active sector of the Tracker under realistic cabling and grounding conditions, establishing the data acquisition, and confirming stable and safe operation under the supervision of the dedicated monitoring systems. The objectives were also to develop and validate monitoring tools, to identify issues in service routing or connections, to establish stable and safe running at low temperature, and to demonstrate operating procedures. Finally, the acquisition of cosmic ray data allowed the measurement of the detector performance, the understanding of tracking algorithms, and to perform an initial alignment of the active modules.

The test progressed in an incremental way, beginning with testing of parts of the sub-systems, then proceeding to a test of the barrel systems, and finally incorporating one endcap. There were also short system tests to check for any interference between the Tracker and a small fraction of the forward pixels: these tests, which are not described in this note, did not show any interference effects.

The Sector Test provided an important opportunity to evaluate Tracker performance in some detail and address any weak points. Several million cosmic ray events were taken under a range of conditions, operating the Tracker over a range of temperatures, from 15 °C down to -15 °C.

The results obtained from the Sector Test are described in three dedicated papers. This note documents results on the detector performance while results on track reconstruction and alignment are described in Ref. [4] and Ref. [5] respectively.

The Sector Test setup is described in Section 2. The data sets, reconstruction and processing are presented in Section 3, while Sections 4 and 5 are concerned with the detector performance. Section 6 covers the generation of the cosmic muons in the Tracker and the simulation of the detector response. The tuning of key parameters in Monte Carlo simulation studies to match the data is the subject of Section 7.

2 Sector Test description

The Silicon Strip Tracker has a barrel region with four layers in the TIB and six layers in the TOB, and a forward region with three disks in the TID and nine in the TEC on each side of the Tracker. Each TID and each TEC disk is organized in three and seven rings respectively, where each ring corresponds to a different radial range and

Table 1: Composition of the Sector Test with the different subdetector layers/disks.

Tracker Sub-detector	Number of Modules	Number of Channels	Fraction of Tracker
TIB	438	282 624	16%
TID	204	141 312	25%
TOB	720	476 460	15%
TEC	800	483 328	13%
Total	2162	1 383 424	15%

different module geometries. For the Sector Test a fraction of the Tracker was powered and read out using the APV25 front-end chip [6, 7], selected so as to maximize the crossing of all the different layers or rings by cosmic rays. The first quadrant in the Z+ side of the Tracker was chosen. Details of Sector Test sub-detectors are shown in Table 1. Sensors were biased with a voltage of 300 V for TIB, TID and TOB, and 250 V for TEC.

The analog signal from the silicon sensors is amplified, shaped and stored in a 192 element deep analogue pipeline every 25 ns. A subsequent stage can either pass directly the pipeline signal (Peak mode) or form a weighted sum of three consecutive samples effectively reducing the shaping time to 25 ns (Deconvolution mode): only results obtained with APV25 in Peak mode have been thoroughly studied at the Sector Test and therefore no Deconvolution mode results will be described. The signal is then multiplexed by the front-end chip APV25. In order to approach the behavior of an ideal CR-RC circuit with a 50 ns shaper, the APV25 settings can be optimized depending on the value of input capacitance and operating temperature. Laboratory studies [7] were made to evaluate the optimal settings for specific geometries over a range of temperatures which were used during the Sector Test.

The signals from each APV25 channel are amplified, converted to light by an Analog Opto Hybrid (AOH) [8] and sent via optical fibers to the Front End Driver board (FED) [9, 10] where they are digitized and further processed, prior to transmission to the central DAQ system. Data can be taken in two different modes: Virgin Raw (VR) or Zero Suppressed (ZS). In VR mode, all channels are read out with the full 10 bits ADC resolution. In ZS mode, the FED applies pedestal subtraction, common mode rejection and a fast clustering algorithm, using signal height with a reduced 8 bits resolution: only channels forming a cluster are output. Almost all cosmic ray data were taken in Virgin Raw mode since the low cosmic trigger rate did not require data reduction, and VR running allowed offline optimization of thresholds.

Clock, trigger signals, and slow control communication with the front-end electronics are managed by the Front End Controller (FEC) boards [11] and sent via optical fibers to the Digital Opto Hybrid (DOH) [12, 13] for each control ring of the Tracker: signals are distributed by the DOH to every Communication Control Unit (CCU) [14] in a control ring. Finally each CCU sends signals to Tracker modules, in particular clock and triggers via a Phase Locked Loop (PLL) circuit on each module [15]. It receives monitoring data provided by each module from the Detector Control Unit (DCU) chip [16].

FEDs and FECs were read out during the Sector Test via VME bus, rather than the high speed S-Link interface to be utilised in CMS. The DAQ software developed to configure and manage readout of Tracker data is based on XDAQ applications [17] which also provided algorithms to commission the detector [18].

The services needed consisted of 277 LV/HV cables, 52 control cables, 73 optical fiber cables and 32 cooling loops. The electronics racks required 145 power supply modules, 17 power supply control modules, all of which were units from the final system [19], 65 FEDs and 8 FECs for a total of 41 control rings.

The cooling plant used for the Sector Test was simpler than the final system and its cooling power limited. A minimum operating temperature of -10°C was obtained, compared to -25°C in the final system. The temperatures measured at the cooling tubes proved to be very stable with variations of less than 0.1°C . A test was possible at a temperature of -15°C but only by limiting power to half of the Sector Test modules.

Dry air was supplied inside to maintain a sufficiently low dew point to avoid condensation; it flowed in a semi-hermetic tent that contained the Tracker.

2.1 The Tracker Safety and Control Systems

The Tracker Safety system (TSS) [20] is designed to guarantee protection of the Tracker. It is self-contained and operates on information provided by a thousand hardwired sensors. A system based on Programmable Logic

Controllers (PLC) handles the process of monitoring those sensors and taking actions depending on the monitored values, which consist of digital values of temperatures, humidities and TIF, or CMS cavern, information. The TSS will interlock the Tracker power according to a user defined scheme when either a single temperature sensor or a group of sensors varies outside user-defined safety limits, or when the TIF or cavern systems fail to respond. During the Sector Test two TSS sections, out of the final six, were fully functional and the Tracker was reliably interlocked on several occasions on over-temperature, cooling plant failure, power cuts, or other alarm conditions.

The Tracker Control System (TCS) [20, 21] handles all interdependencies of control, low and high voltages, as well as fast ramp-downs in case of higher than allowed temperatures and currents in the detector, or in case of general unsafe conditions detected in the experiment cavern. The size and complexity of the CMS Tracker imposes several demands on the control system to ensure the safety and operation of the modules; the TCS evaluates about 10 000 power supply parameters, nearly 1000 parameters from TSS and 100 000 parameters from the DCUs situated on all front hybrids and CCU modules. The TCS should intervene before the TSS system enters into action, allowing a gentle switch off of parts under risk, and with a finer granularity than the TSS. During the Sector Test about 20-25% of the final system was controlled by the TCS/TSS.

The basic software building block is the commercial SCADA (Supervisory Control And Data Acquisition) software PVSS (Prozess- visualisierungs- und Steuerungssystem by ETM [22]). This has been greatly extended by CERN in a common LHC framework, adapting it to the needs of individual experiments by incorporating local modifications. The LHC features also extend functionalities such as archiving of values and the treatment of alarms, warnings and error messages.

The Sector Test enabled final implementation of the full TCS to PLC communication including the downloading of parameters, such as sensor limits and sensor-group to interlock-grouping, to the PLC. Complete calibrations inside PVSS were established, including all ADC to physical value conversions. Several additional checks were introduced from PVSS to PLC programming: for example, a minimal number of sensors should participate in interlock voting or limits required to stay in a sensible region. A full checkout interlock routine was developed.

The complexity of the TCS system required a network of PCs for the distribution of requests. The Sector Test was the perfect test bed to establish, check, and tune the distribution needed for the final system as performance needs for the Sector Test were very close to those of the final system. The main bottleneck was found to be memory but the OPC performance of the CAEN system was also identified as a critical item.

2.2 Cosmic Muon Trigger

The cosmic trigger configuration was designed to allow studies of tracking performance and detector alignment. The trigger design was constrained by space above and below the Tracker; in particular clearance below the Tracker allowed only 5 cm lead bricks for filtering low momentum tracks. Six scintillators (T1, T2, T3, T4, T5, T6) were placed above the Tracker, in a fixed position; below the Tracker there was initially only one scintillator (B0) mounted on a movable support structure; later a further set of four scintillators was added (B1, B2, B3, B4) to increase the trigger acceptance. The dimensions and the single trigger rates of all scintillators are shown in Table 2.

The upper scintillator signals were synchronized by simple NIM logic using cosmic rays and put in a logical-OR to obtain a Top-scintillator signal. This was put in coincidence with the lower scintillator signal. The coincidence rates are shown in Table 2. From the entries it can be seen that efficiency of the upper scintillators was not uniform.

In the same way from synchronized logical-OR signals of scintillators B1, B2, B3, B4 a Bottom-scintillator signal was obtained and was put in coincidence with the Top-scintillator signal. The rates are shown in Table 2. They show good performance: the discriminator threshold allowed to obtain a very uniform coincidence rate.

Three main trigger configurations have been used at the Sector Test: (TA)= (Top-Scintillator & B0) vertical position; (TB)= (Top-Scintillator & B0) slanted position; (TC) = (TA) plus (Top-Scintillator & Bottom-scintillator) slanted position. The schematic representations of these three configurations are shown in Fig. 1. The rate of spurious coincidences relative to the true level was of order 10^{-9} . The trigger rates achieved were: 3.5 Hz (TA), 1.5 Hz (TB), and 6.5 Hz (TC). Since the DAQ rate was limited to about 3 Hz by the FED readout via VME, a trigger veto was implemented to keep the rate under this level.

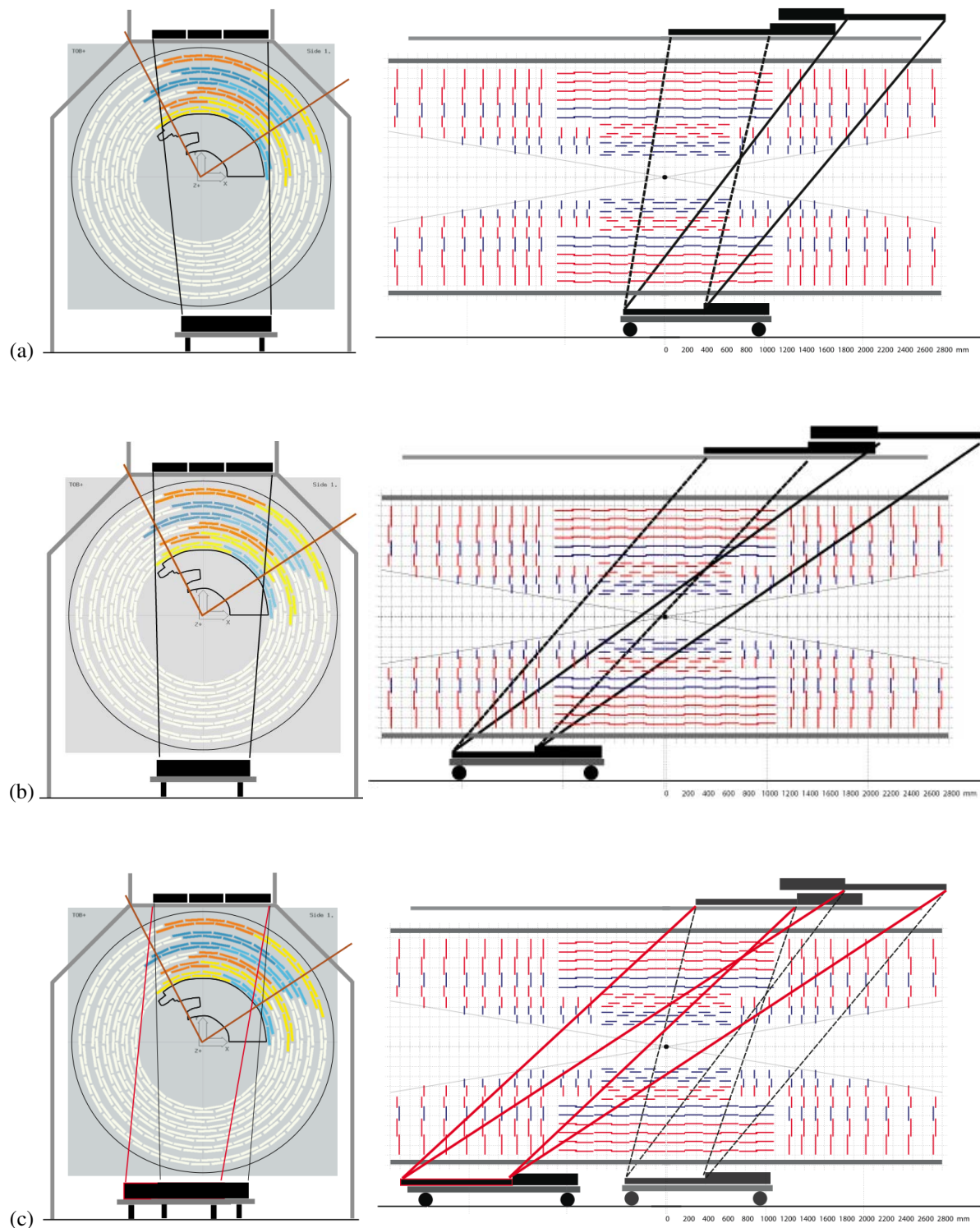


Figure 1: Layout of the various trigger scintillator configurations used during the cosmic data taking at the TIF (in chronological order): (a) configuration TA; (b) configuration TB; (c) configuration TC. The xy view is shown on the left side, the rz view is shown on the right. The straight lines connecting the active areas of the top and bottom scintillation counters indicate the acceptance region.

Table 2: Dimensions of scintillators used at Sector Test; single and coincidence rates.

Scintillator	DX (cm)	DY (cm)	Thickness (cm)	Single Rate (Hz)	Rate on coincidence (T _i & B0) (Hz)
T1	30	100	0.8	80	0.42
T2	30	100	0.8	60	0.93
T3	40	80	0.8	72	1.67
T4	30	100	0.8	85	0.42
T5	30	100	0.8	97	0.18
T6	40	80	0.8	110	0.62
B0	75	85	2	235	-
Scintillator	DX (cm)	DY (cm)	thickness (cm)	Single Rate (Hz)	Rate on coincidence (B _i & Top-Scint.)(Hz)
B1	40	110	2	260	0.45
B2	40	110	2	275	0.45
B3	40	110	2	290	0.45
B4	40	110	2	240	0.45

3 Data sets and reconstruction

The division of the data in different sets, is detailed in Table 3, where run number intervals are specified for the participating detectors, the trigger configurations, and the operating temperatures. The APV25 parameters listed in the table are for specific hybrid temperatures (T_{APV25}) and were studied for TIB and TOB detector modules only. For the TID and the TEC (where a large number of variants exist) the APV25 parameters have not been optimized for each module type. Instead the TID used the TIB parameters while the TEC used parameters very close to those of the TOB.

Each run was checked using online and offline data quality monitoring tools. If a run did not meet the quality requirements or if a configuration or hardware problem was discovered, it was flagged as bad and excluded from the offline analysis.

Table 3: Sector Test data sets.

Run	Detector	Trigger	Operating T (°C)	Total Events	Good Events	T_{APV25} (°C)
6203-6930	TIB TID TOB	A	15	703 996	665 409	30
7277-7296	TIB TID TOB TEC	A	14	191 154	189 925	30
7635-8055	TIB TID TOB TEC	B	14	193 337	177 768	30
9255-9341	TIB TID TOB TEC	C	14	132 311	129 378	30
10145-10684	TIB TID TOB TEC	C	10	992 997	534 759	30
10848-11274	TIB TID TOB TEC	C	-1	893 474	886 801	10
11316-11915	TIB TID TOB TEC	C	-10	923 571	902 881	10
12045-12585	TIB TID TOB TEC	C	-15	656 923	655 301	0
12599-12656	TIB TID TOB TEC	C	14	112 139	112 134	30

3.1 Reconstruction

Event reconstruction, event selection, data quality monitoring, simulation and analysis of the Tracker Sector Test at the TIF were performed within the CMS software framework known as CMSSW[23]. Hit and track reconstruction was performed offline taking the raw data or the simulation data as input. A reconstruction job is composed of a series of applications executed for each event in the order specified by a configuration file. A fundamental part of the processing is the availability of non-event data such as cable map, pedestal, alignment constants and calibration information.

The first step consists in mapping ADC counts for individual strips as they are coming from the FED output, into objects that are uniquely assigned to a specific detector module exploiting the cabling map information stored in the configuration database. In the case of data collected without performing online zero-suppression (VR), the necessary pedestal information must be acquired from the database. At this point, the input data files, whether real data or Monte Carlo simulated events, contain the same information and can be further processed with identical

code.

A three-threshold algorithm, described in detail in the CMS Physics TDR[23], is used to form clusters. The cluster seed is defined as a strip whose charge is at least three times greater than the strip noise, while neighboring strips are added if their charge exceeds twice their strip noise. The cluster is kept if the total cluster charge is more than five times the cluster noise level, defined as the quadratic sum of all the strip noise values. Finally, the position of the cluster is calculated as the centroid of the individual strip charges.

Three tracking algorithms have been applied: the Combinatorial Track Finder, the Road Search and the Cosmic Track Finder. The Combinatorial Track Finder and the Road Search are reconstruction algorithms developed for $p - p$ collisions, while the Cosmic Track Finder is a specialized code for reconstruction of single cosmic track events [4]. The input to the tracking algorithms are reconstructed hits as described above and information from the alignment constants (either from survey or from alignment calibration studies).

All the tracking algorithms employ the same three steps: seeding, pattern recognition and track fitting. The seeding and the pattern recognition are specific to each algorithm, while the final fit is the same for all of them. Since no magnetic field was present the tracks are extrapolated as straight lines. Material effects, energy loss and multiple Coulomb scattering are estimated each time a track crosses an active layer. The amount of material at normal incidence is estimated via the reconstruction geometry developed for $p - p$ collisions. Since the momentum of the track is not measured, a constant value of $1 \text{ GeV}/c$ is assigned, close to the expected average from simulation.

More detailed information about the algorithms and their performance can be found in Ref. [4]. All the results presented in sections 5, 6 and 7 of this paper refer to tracks obtained only with the Combinatorial Track Finder algorithm to avoid duplication of information.

3.2 Data Quality Monitoring

The Data Quality Monitoring (DQM) system for the Tracker is designed to ensure that good quality data are recorded and detector problems are spotted very early on. The system is based on the “Physics and Data Quality Monitoring” framework [24] of CMS. The task is fulfilled in three steps : (a) histograms, called Monitoring Elements (MEs), are defined and filled with relevant event information by the “Producer” (DQM Source) application; (b) a “Consumer” (DQM Client) application accesses the MEs, performs further analysis and generates alarms; and (c) the “Graphical User Interface” (GUI) provides tools for visualization of the MEs.

The MEs are defined in the DQM source at various levels of data reconstruction chain. Starting from the level of pedestal, noise, digitization, cluster reconstruction and finally track-related properties are defined and filled in various MEs.

The DQM Client accesses low-level MEs and performs further analysis on them and creates summary MEs, performs quality tests comparing MEs with references to generate alarms. The summary plots are important as it would be too time consuming to check each of the huge set of MEs in the Tracker, which consists of over fifteen thousand detector modules. The information from detector level MEs is accessed and summarized in MEs at higher levels following the geometrical structure. Similarly the detector level MEs are compared with reference MEs or parameters and “Ok”, “Warning”, and “Error” alarms are generated, as appropriate, based on the comparisons.

The DQM system was operational with full functionality during TIF data taking. Events were accessed from the on-line data and full reconstruction was performed on an event by event basis and provided to the DQM sources. The system was stable during operations and the Tracker DQM GUI, which is a web based application, was accessible from CERN as well as from other institutes involved in the Tracker activities.

3.3 Data Processing

The tracker data processing consisted of the following steps: data archiving, conversion of data from the raw format to the CMS Event data Model (EDM) format based on ROOT[23], registration in the CMS official data bookkeeping services, transfer to remote computing tiers, data reconstruction and analysis in a distributed computing environment.

Data taking and analysis needed a large amount of available disk space, since both raw data and on-site local analysis results had to be stored centrally in a safe way. The design chosen for the computing model was a centralized one, where all the data are stored on a single machine which is connected via NFS to the local network. A room containing all PCs and local storage was equipped to allow the data taking control, monitoring and first analysis of the data and it is referred to as the Tracker Analysis Center (TAC).

All the data collected by the tracker detector were written into a main storage machine at the TAC, which behaved like a temporary data buffer. Data were backed-up to CASTOR storage at CERN every five minutes, copying data files only when they did not exist on CASTOR side and had not been accessed in the last hour (to prevent the copy of data still being modified). Once all the files belonging to a run were copied to CASTOR, a catalog was prepared for that run after a few checks. Because of the limited resources at TAC and following the CMS computing and analysis model, most of the processing of the data was done in remote sites as soon as data were officially published and transferred to them. The transfer was performed to remote sites using the CMS official data movement tool PhEDEx . Tracker data were transferred and registered successfully at Bari, Pisa and FNAL.

The datasets have been reprocessed several times to feed back into the reconstruction phase the improvements in the alignment and calibration corrections obtained from the analysis. The final reprocessing was performed in FNAL in December 2007.

4 Detector Performance based on Calibration Data

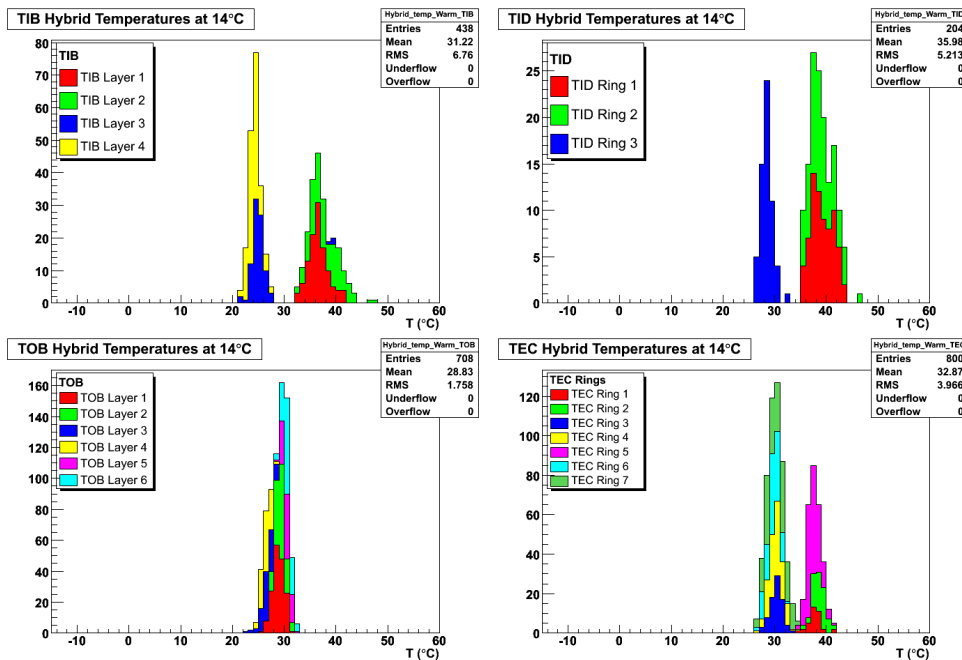


Figure 2: Hybrid temperature distributions for TIB, TID, TOB, and TEC at a coolant temperature of 14 °C.

The performance of the Tracker depends on front end electronics supply voltage and operating temperature. These quantities are measured by the DCU chip located on each module hybrid, which can be read out digitally via the control ring protocol through the electronic chain (DCU, CCU, DOH, FEC).

Results obtained for the hybrid temperature are shown in Fig. 2 and for sensor temperature in Fig. 3 for 14 °C coolant temperature. All TOB layers show the same temperature, while for TIB, TID and TEC differences are visible: TIB layers 1 and 2, TID ring 1 and 2, and TEC ring 1, 2 and 5 are double-sided layers and have a temperature substantially higher compared with single-sided layers; the effect is more pronounced for the hybrid than for the sensor. These differences are expected to be lower with the final cooling system.

It is also apparent that three modules of TIB layer 3 have a higher temperature of about 15 °C; they are in a string where the cooling pipe was blocked. Results from the other operating temperatures are consistent with those obtained at 14 °C.

The power supply system provides 2.5 V and 1.25 V lines to the modules, correcting for voltage drops along the long power supply cables by sensing the voltage levels as close to the modules as possible. Nevertheless, there still remains a small cable resistance which causes a non-negligible voltage drop. The operating voltage of the modules is measured by the DCU and results are shown in Fig. 4 for the 2.5 V line and in Fig. 5 for the 1.25 line. The average is below nominal for all layers of sub-detectors. These measurements show that it is possible to evaluate these voltage drops and therefore to eventually better equalize the module voltages to match the requirements.

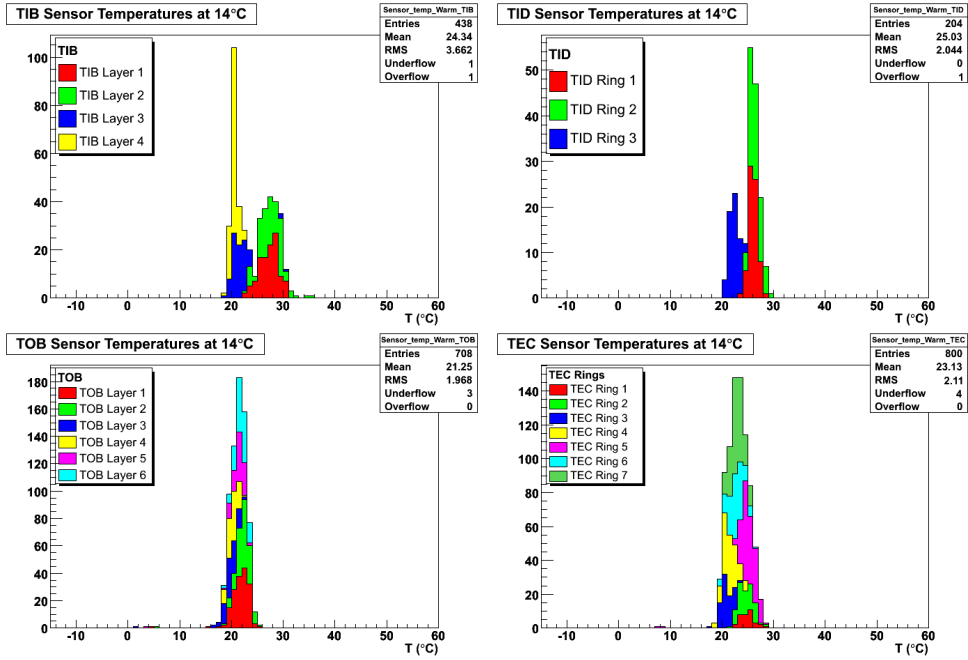


Figure 3: Sensor temperature distributions at a coolant temperature of 15 °C for TIB, TID, TOB, and TEC.

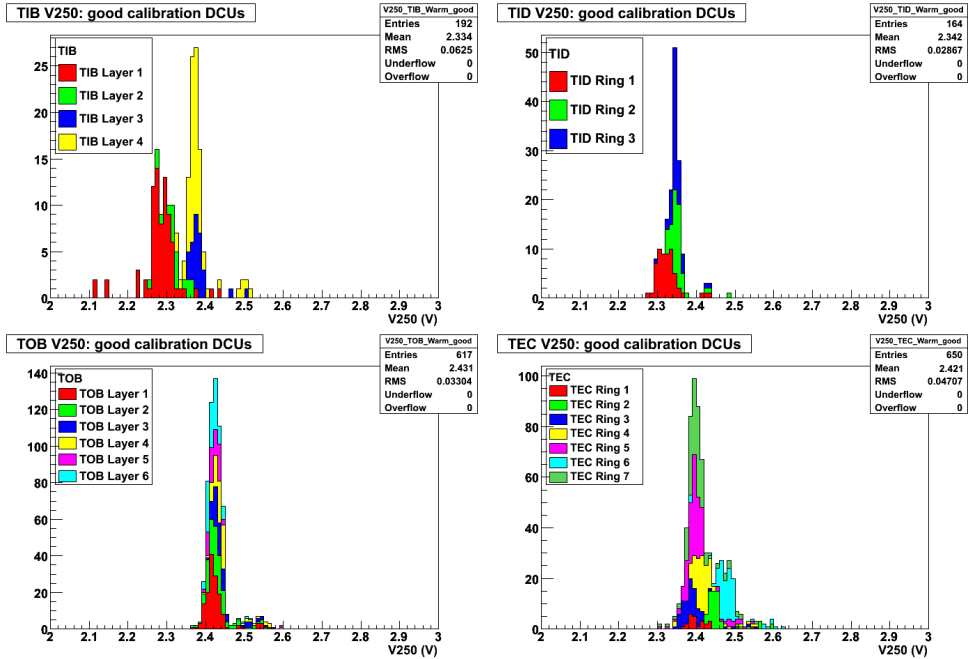


Figure 4: 2.5 V voltage line value measured at the module for TOB, TIB, TEC, and TID.

4.1 Electronic Gain Measurements

This section describes how the electrical gain of the Tracker system is both determined and adjusted, that is, the procedures by which the gains of individual APV25s are adjusted to a common and known value. The readout chain for the Tracker involves pairs of adjacent APV25s, the hybrid MUX, the AOH [8], an optical fiber, and the FED [9]. Instabilities in the low or high voltages or changes in temperature can affect the gain. Measuring the electrical stability of the Tracker as a function of time, voltage, temperature, and other variables, should lead to an improved understanding of the likely performance of the full Tracker system during actual LHC operations.

The commissioning procedure [18] determines optimal settings of the electronics to achieve a uniform electronic

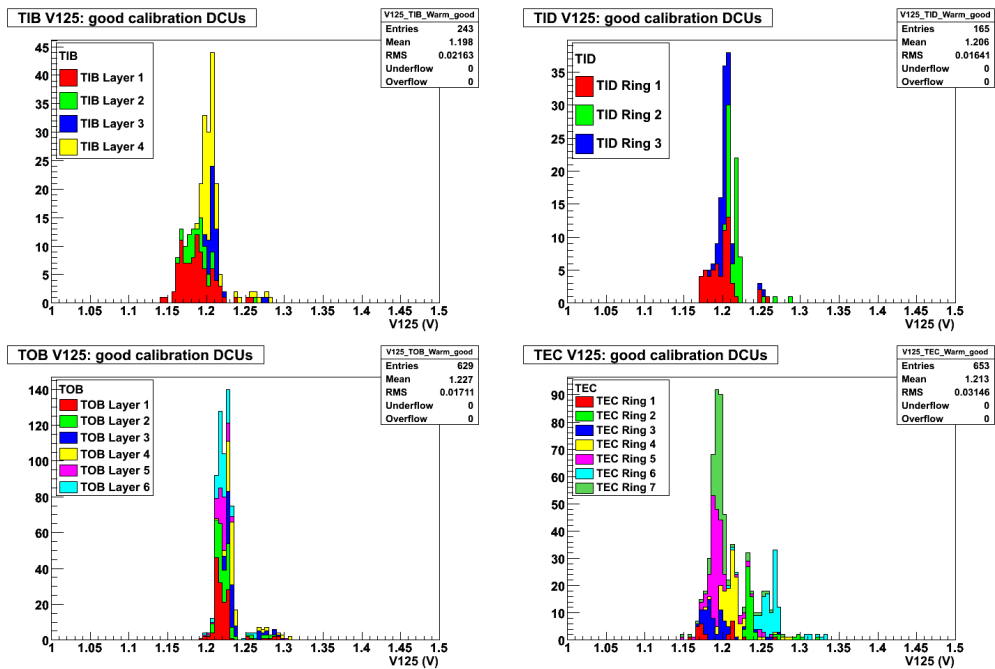


Figure 5: 1.25 voltage line value measured at the module for TOB, TIB, TEC, and TID.

gain. This is obtained by measuring the value of the height of synchronization pulses, referred to as tick-marks, generated by the APV25 which provide a stable value that can be used as reference to equalize the response of the full electronic chain. It is required that the tick-mark height of each APV25 be within the FED dynamic range and, by varying the AOH offset and gain, should correspond closely to the target value of 640 ADC channels. The full commissioning procedure was consistently applied whenever there were changes in coolant temperature, changes in APV25 parameters, or in the hardware configuration. Commissioning runs, referred to as timing runs, provide precise measurements of the tick-mark heights, therefore of the electronics gain, and were repeated at intervals between full commissioning runs to get more statistics on stability of the system.

Tick-mark height distributions obtained after the commissioning procedures are shown in Fig. 6. The several gray levels represent the components with different AOH gain settings (called 0, 1, 2, 3 from lower to higher gain): the difference between the left and right distributions is mainly due to the strong dependence on the temperature of the AOH gain. The effect is manifest by the increased number of AOH with gain equal to 0 at lower temperature. This implies that the average values of the tickmark height distribution changes when varying the temperature.

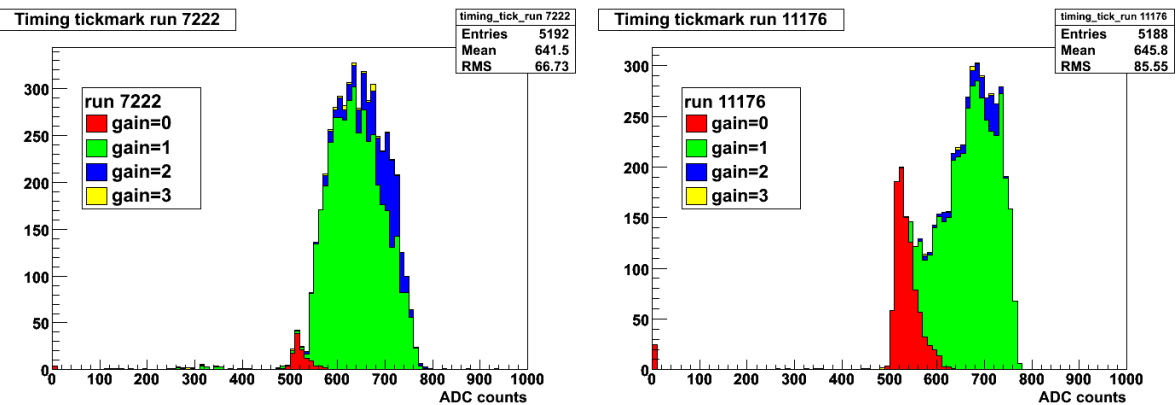


Figure 6: APV25 tickmark height distribution after commissioning procedure: run 7096, taken at $T = 14^\circ\text{C}$ (left), and run 11176, taken at $T = -10^\circ\text{C}$ (right).

Even after the commissioning procedure the tickmark height distributions still indicate about a 10% spread in electrical gain. This variation is consistent with the coarse precision of the AOH laser gain settings. An offline

calibration of the electronic gain is necessary to improve the precision of the measurement of noise and signal. This is achieved by normalizing to an assumed digital header of 640 ADC counts. In the following sections, the analysis of signal and noise will take into account this calibration if not otherwise stated, by applying a correction factor of

$$C_{corr} = \frac{640}{TickMark}; \quad (1)$$

One limitation in the use of this equation is due to the different module operating voltages for different layers. It was known that the tick-mark amplitude is linearly proportional to the 2.5 V operating voltage, therefore tickmarks from different modules can be compared only if they operate at the same voltage. The signal at the APV25 amplifier output is not much affected by changes in the supply voltage. Therefore to make a more precise estimate of the electronic gain it is necessary either to equalize all the operating voltages or to correct the tick-mark value for the difference compared to 2.5 V. In this paper this correction was not applied therefore the electronic gain can be considered having a systematic variation of about 5% that affects direct comparison between different layers.

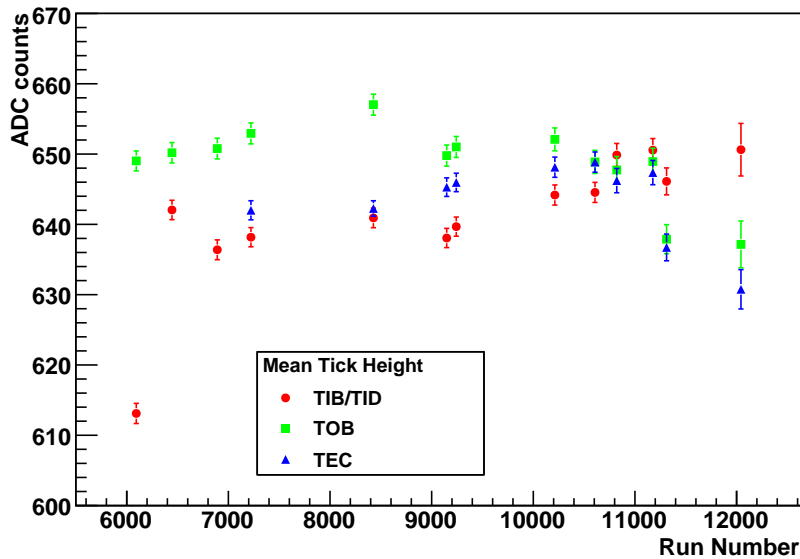


Figure 7: Tickmark height distribution versus run number. Error bars represent the statistical error of the average value.

It is important to understand the stability of the electronics gain, since calibration runs are taken only at selected times. In the analysis of the timing runs, bad modules have been discarded and a selection of good commissioning runs have been made. Figure 7 shows average tick-mark heights for individual sub-detectors as a function of run number (with the help of Table 3 the period at different temperatures can be identified). At least one timing run was taken as part of the commissioning procedure whenever the coolant temperature changed. During the period at $T = 14 - 15^\circ\text{C}$, in particular, there were several timing runs, which provide information on the stability of the system.

TOB shows, in 7 runs, variations of $\pm 0.6\%$. The TIB/TID shows a large discrepancy in the first run (6094), where results are lower by 5%, but this is due to the fact that the modules were operating at low electrical gain and therefore that was corrected by a very high AOH gain: after removing this run the TIB shows, in 6 runs, variations of $\pm 0.6\%$. The TEC shows, in 4 runs, $\pm 0.4\%$ variations.

4.2 Noise Performance Studies

Prior to irradiation, the noise of a module is almost completely determined by the input capacitance load at the APV25, which in turn is dominated by the silicon strips. Thus, within 8%, one expects a linear dependence of the noise on the length of the silicon strip for all modules.

In the Sector Test, modules were mounted on the final support structures and therefore were in close proximity to each other, which could have exposed APV25 inputs to other sources of noise. In particular grounding loops, cross-talk from neighboring modules or other noise sources, (digital noise, cables, power supply) could have affected

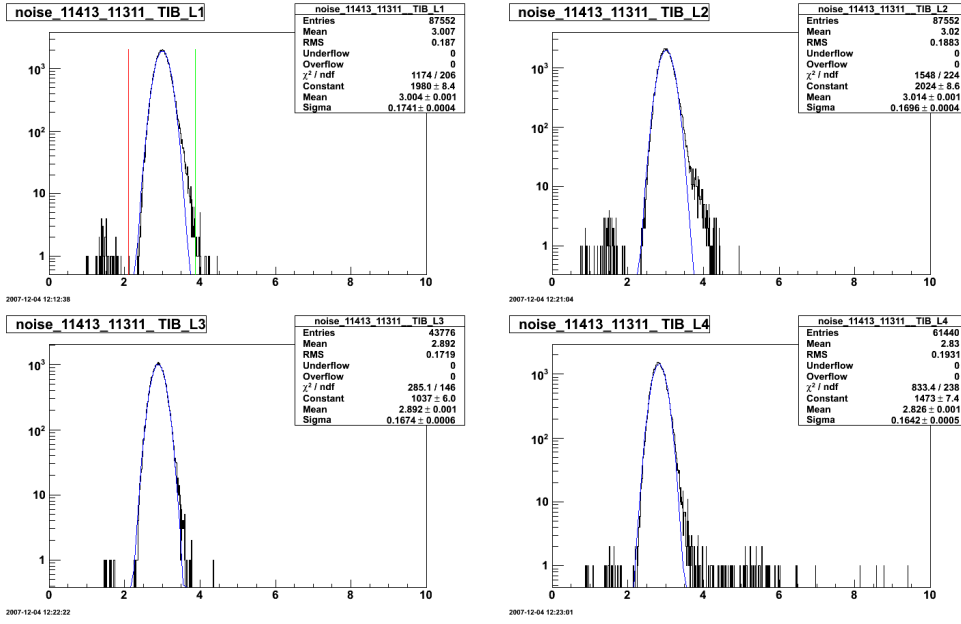


Figure 8: TIB noise profile for $T = -10^\circ\text{C}$ for layers 1, 2, 3, and 4. Gaussian fit is shown. X axis is ADC value.

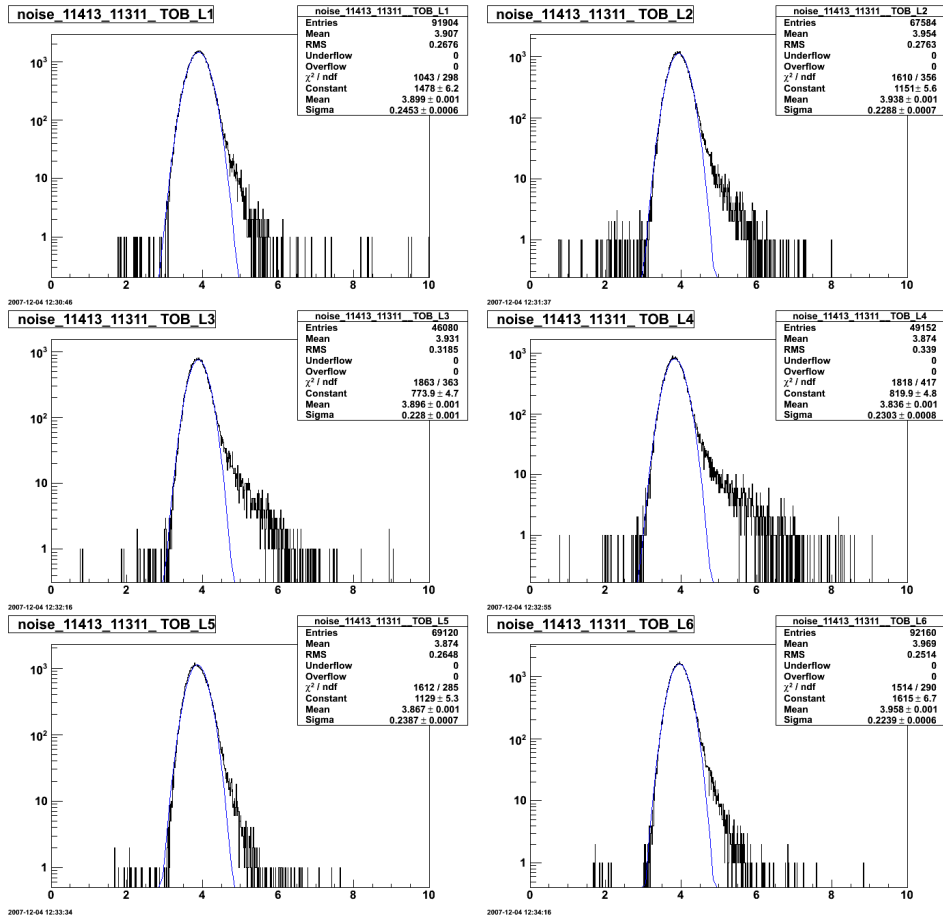


Figure 9: TOB noise profile for $T = -10^\circ\text{C}$ for layers 1, 2, 3, 4, 5 and 6. Gaussian fit is shown. X axis is ADC value

the final noise performance. Moreover, a study of the temperature dependence is important. The commissioning procedure plays an important role, since it optimizes many system parameters and consequences are observed

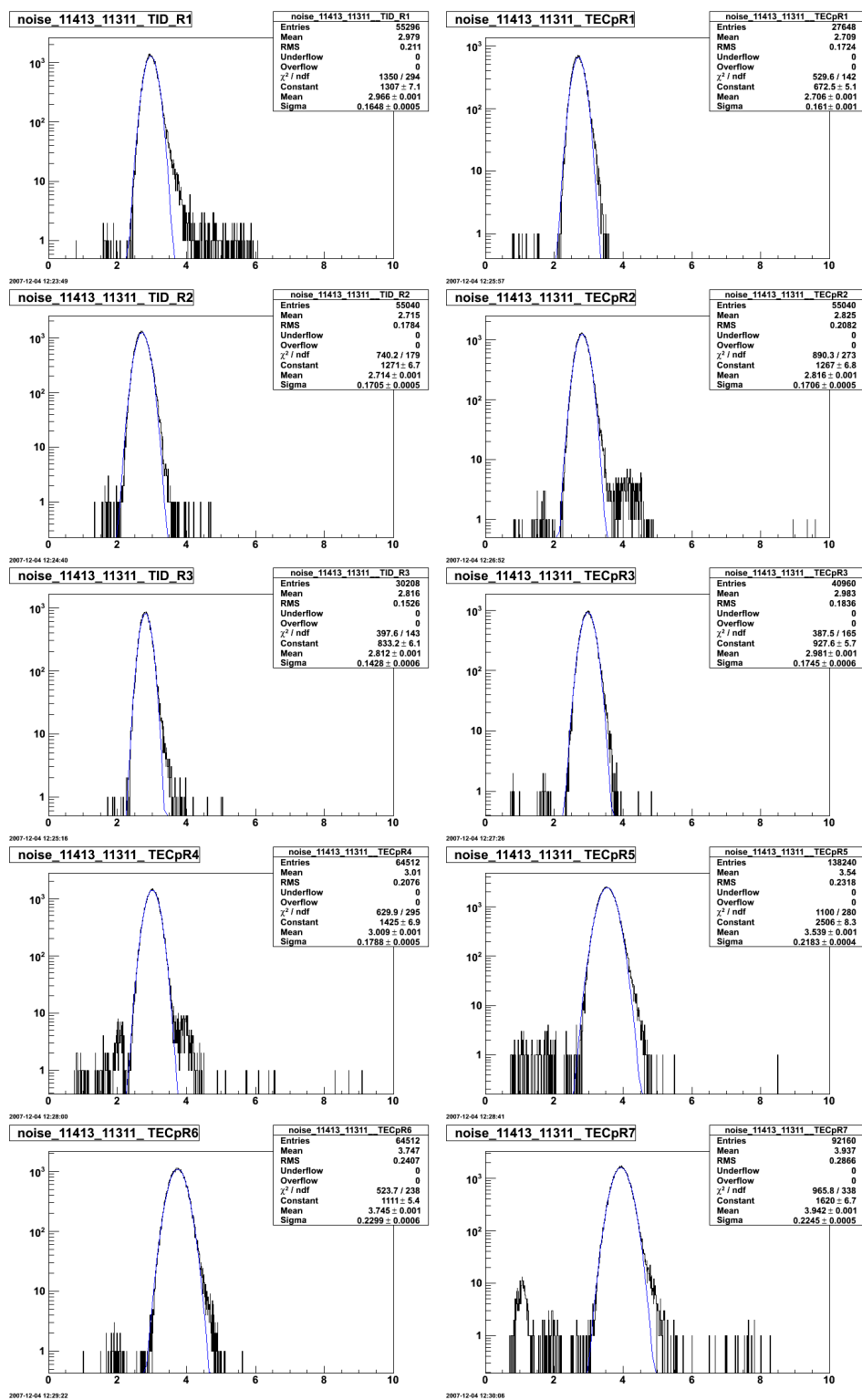


Figure 10: Noise profiles for $T = -10^\circ\text{C}$ for different rings of TEC and TID. Gaussian fits are shown. R2 and R3 silicon geometries are the same for TID and TEC. X axis is ADC value

on the noise performance. In the following the noise has been renormalized for each pair of adjacent APV25, belonging to the same AOH laser, in order to take into account the different electronic gains, by multiplying the noise for the correction factor specified by equation 1.

Modules with known problems that affect the noise distribution calculation have been removed from the analysis at least for the period when the problem was present.

Strip noise distributions for runs taken at -10°C are shown for each layer for TIB and TOB in Fig. 8 and Fig. 9 respectively, while for TEC and TID are shown in Fig. 10. For each distribution, a fit to a Gaussian has been performed and results are shown. For most of the layers the noise distribution is very well represented by a Gaussian, and fitted values and sigmas are almost identical for identical layers, showing extra noise sources do not affect the detector performance significantly.

The only relevant non-Gaussian tails at high values are visible for TOB layers 2, 3 and 4. They are mainly due to channels close to APV25 edges and only for modules at specific positions within a rod, closer to a clock distribution board and a power cable. This noise pickup does not affect the TOB performance, given its high signal to noise ratio, as shown in the next section. Nevertheless, during the Sector Test many possible grounding and filtering schemes were investigated in order to minimize this extra noise. A solution which was found to be very effective consisted in grounding the TOB power cable shields at the patch panel close to the Tracker. This grounding implementation was possible on the Sector Test setup only for a fraction of the TOB, therefore the tails remained for most of the module rods. This grounding scheme has subsequently been implemented during installation of the Tracker inside CMS.

Stability of the noise performance was studied by taking pedestal and noise runs at different times when the Tracker was running in a stable conditions with fixed electronics configuration settings. Results are shown in Fig. 11 displaying noise of all layers/rings versus the run number for TIB and TOB: the steps in values represent the different temperatures considered, 10°C , 0°C , -10°C and -15°C . The data average and mean value of a Gaussian fit are displayed as solid and open symbols respectively. For constant coolant temperature the noise is stable to better than $\pm 0.5\%$. Most importantly, the noise decreases with decreasing temperature as expected by the laboratory studies made on the APV25 performance.

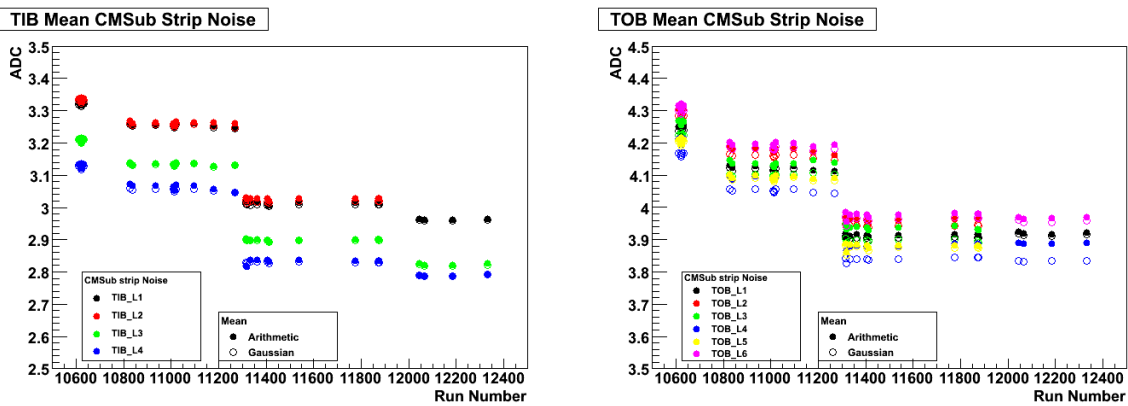


Figure 11: Noise vs run number for TIB on the left and for TOB on the right. Four periods at different temperatures are visible: 10°C , 0°C , -10°C and -15°C

The (Gaussian fit) mean strip noise obtained for each different type of module has been correlated with the module strip length. Results are shown in Fig. 12 for a run taken at -10°C , but similar results are obtained at the other temperatures. Error bars represent the spread of the mean module noise for each module type. As expected the behavior is well represented by a linear behavior, within statistical fluctuation, for modules from the same layer, although the average values show differences for the same strip length but different module geometries. This can be explained by the difference in supply voltage and by the different APV25 settings used for different sub-detectors.

4.3 Detector quality

Faulty channels have been studied both from the perspective of badly behaving modules or missing fibers and of individual bad channels.

Modules with known problems or that were badly behaving were removed either from DAQ or from the data analyses. The resulting fraction of missing modules was at the 0.5% level. Dead fibers were identified during timing runs based on low tick-mark heights. They correspond to the broken fibers whose channels showed problems during the timing runs. The number of missing fibers in the Tracker was at the 0.1% level.

Remaining isolated bad channels were identified having higher than five sigmas, referred as noisy, or lower than

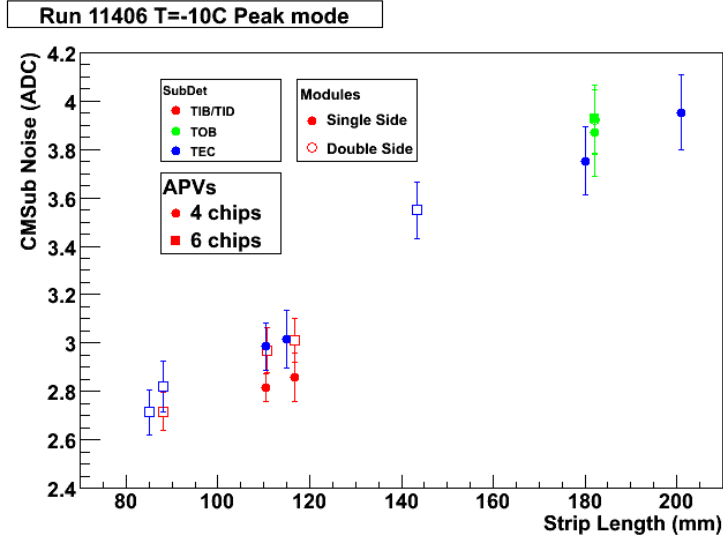


Figure 12: Noise vs strip length for $T = -10^\circ\text{C}$.

five sigmas, referred as dead, noise compared to the average noise per module, and this was done for each module geometry of the Tracker.

The results of this analysis as a function of the run number are shown in Fig. 13. The number of dead channels is almost constant among several runs for all sub-detectors, showing that the identification of dead channels is clear and stable. The noisy components are instead subject to fluctuations, in particular for TOB and TID. The fraction of dead (noisy) strips is 0.05% (0.04%) for TIB, 0.04% (0.15%) for TID, 0.04% (0.3%) for TOB, and 0.08% (0.02%) for TEC.

Since the analysis of defective strips is made on a per run basis, it is important to understand the number of runs in which a strip was identified to be bad. Dead strip identification is stable: the majority of dead strips (70%) were flagged in all runs. About 30% of the classified dead strips appear only in a single run which likely had a timing issue or other unusual problem. On the contrary, only a small fraction of the noisy strips were noisy throughout the Sector Test. In most cases anomalous noise persists for one or two runs at the most. These runs may reflect special operating conditions or non-optimal system configuration.

Finally, a comparison of the identified faulty channels with data from the Tracker construction database shows that 90% of the dead channels and 40% of the noisy channels had been flagged as such by the end of the construction period.

5 Detector Performance based on Cosmic Ray Data

The signal performance of the Tracker is very important; it depends on several factors: charge collection of the silicon sensors, performance of the APV25 with well defined parameters, performance of the full electronic chain.

A study of cosmic trigger timing is presented in the first subsection, to verify that the maximum signal was taken for all the runs. As tracking efficiency relies on a sufficiently large signal to noise ratio (S/N) on all Tracker modules, it is important to measure the S/N on a layer by layer basis. Moreover, S/N analysis does not depend on the gain calibration. Lastly, analysis of the signal size allows a straightforward comparison of the performance of different layers as a means of determining the absolute gain calibration and measurements of temperature dependence.

In order to obtain a high purity signal, only those hits that are associated with a reconstructed track have been used. The CTF track algorithm was used and only tracks with $\chi^2/d.o.f. < 30$ were considered. Only events with low track multiplicity (less than three) and with a low hit multiplicity (less than 100) were considered.

The energy (S_{tot}) deposited in Tracker modules can be parameterized:

$$S_{tot} = \frac{dE}{dx} tK; K = \frac{1}{\cos(\theta_{3D})} \quad (2)$$

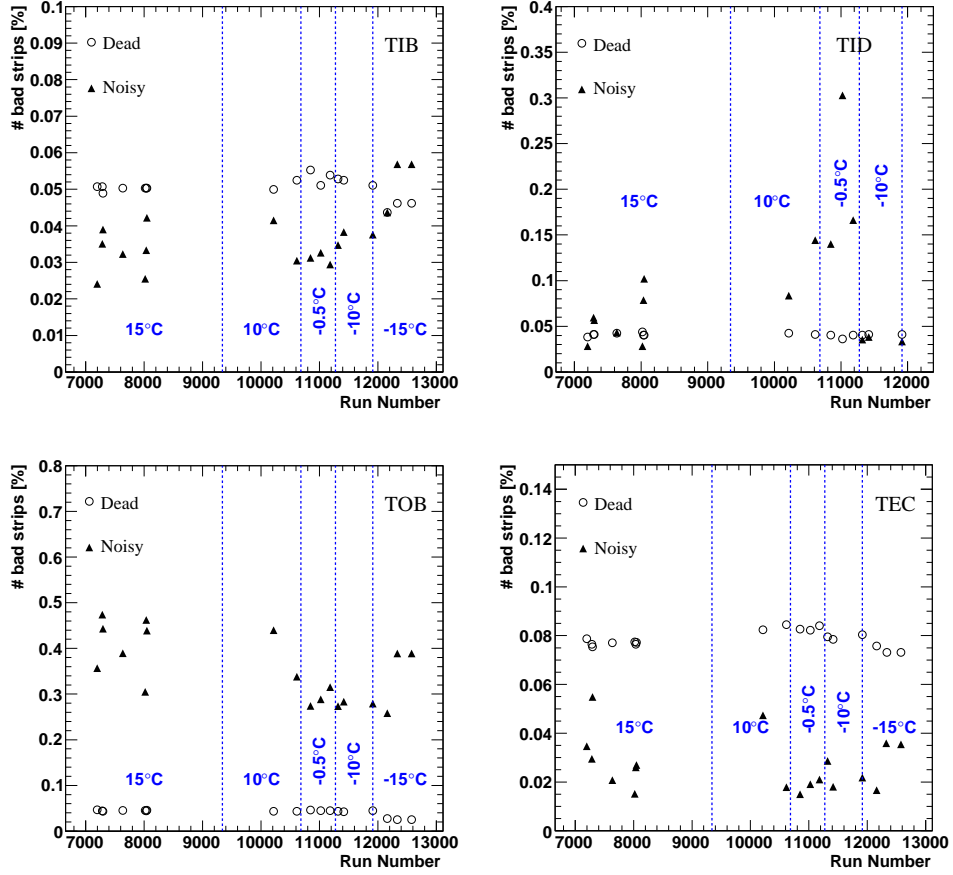


Figure 13: Noisy and dead strips vs run for TIB, TID, TOB, and TEC.

where θ_{3D} is the angle of incidence of the track with respect to the silicon detector normal, see Fig. 14; t is the silicon thickness.

In the following analyses signal values are normalized to the thickness of the silicon detectors.

$$S_{ren} = \frac{S_{tot}}{K} = \frac{dE}{dx} t; \quad (3)$$

Fig. 14 illustrates the definitions of two of the three angles referred to in this section. The XZ angle is angle made by the track in a plane orthogonal to the sensor surface and whose X axis is transverse to the strip direction. There is a direct correlation between the XZ angle and cluster size. The YZ angle is defined in a plane perpendicular to the surface and oriented along the strip direction.

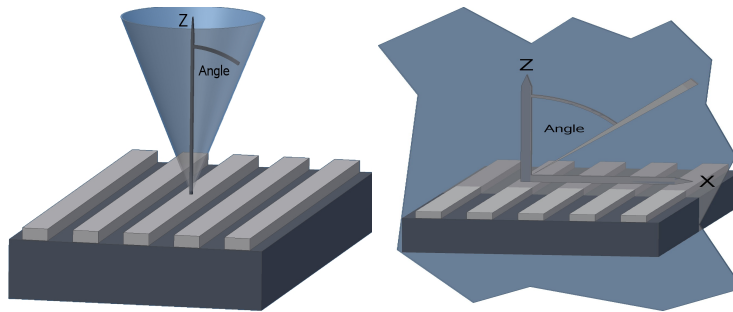


Figure 14: Angle definitions: θ_{3D} on the left; θ_{XZ} on the right.

5.1 Latency Scan

The response of CMS silicon modules to signals is detailed in [25], and only some key points are highlighted in this section. Ideally, the analytical form of the pulse shape in peak mode is the transfer function in the time domain of a CR-RC circuit:

$$S_{\text{peak}}(t) \propto \frac{t}{\tau} e^{-t/\tau}, \quad (4)$$

where τ is the rise time, and the time t is positive. The pulse from the APV25 amplifier lasts about 300 ns, which is large with respect to the 25 ns time which separates two bunch crossings.

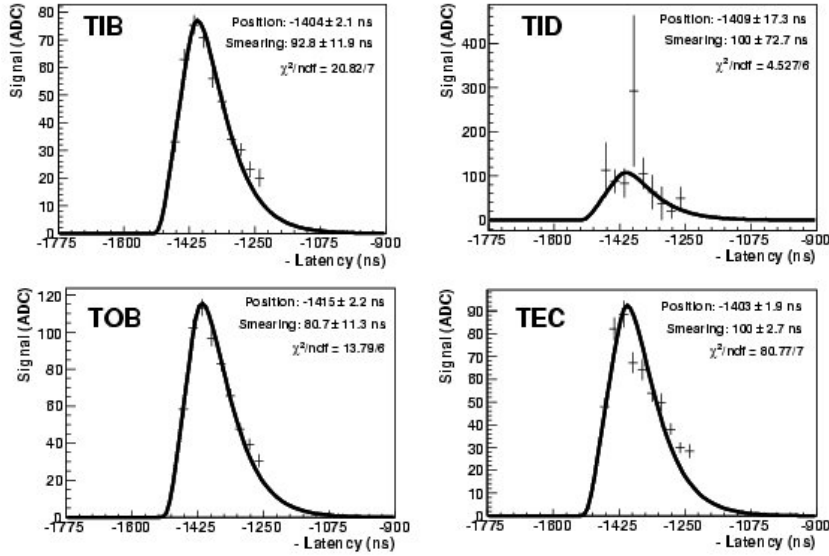


Figure 15: . Fit of the signal as a function of the latency, for each of the four sub-detectors. Data are from run 10947 and were used to set the latency for the following period.

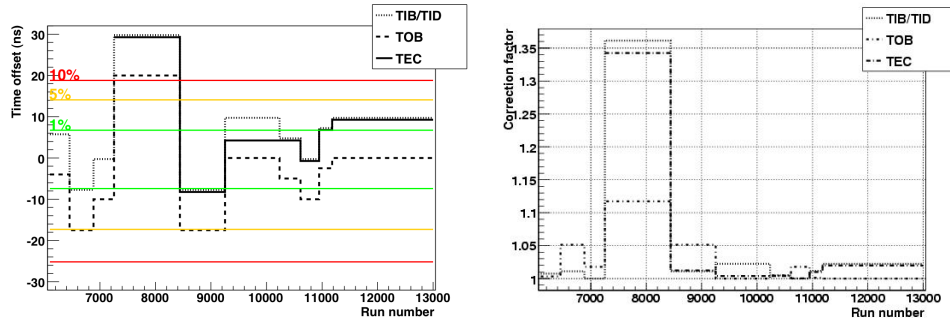


Figure 16: Offset from the on-peak timing (left) and signal correction factor (right) as function of the run number for the three sub-detectors TIB/TID, TOB, and TEC.

The APV25 stores a voltage proportional to the input charge in an internal memory pipeline every 25 ns. The latency of the trigger determines the pipeline cell containing the maximum charge from the traversing particle. This pipeline cell number is the same for all the Tracker modules, since they have been synchronized by the commissioning (*timing*) runs, where the absolute timing of each module is set in order to accommodate the delays introduced by the hardware configuration (fiber lengths, CCU configurations, FEDs, etc.) This is obtained with a precision of 1.04 ns, the time step of the dedicated programmable delay available in the Phase-Locked Loop (PLL), mounted on each module. The PLL allows the independent shifting of the clock and trigger signals.

During the Sector Test, latency scans were done after almost every significant change of APV25 settings or temperature to determine the new latency parameters. Typically about 50 events were taken for each latency step during the scans. About ten steps in latency were performed for a total of about 500 triggers on average.

Results from one of the latency scans are shown in Fig. 15. The latency that maximizes the signal peak for each single subdetector is obtained from fits to these plots. There are small differences in optimal latency among the four sub-detectors due to the different lengths of readout fibers (from the front-end hybrid to the FED). Since no tuning of the pulse shape was performed, deviations from an ideal RC-CR shape are present and therefore a smearing term has been introduced in the fit, to take into account the non-nominal behavior of the pulse shape. The smearing obtained from the fit is larger for TEC, since the pulse shape of individual APV25s was not optimized individually for the many different TEC module geometries.

The estimated difference between the optimal latency and the latency used in the various phases of the TIF Sector Test is shown in Fig. 16. During the many different operating periods of the Sector Test, the commissioning process generally resulted in timing well within a 25 ns window. In one week of running, though, an incorrect latency value was determined by mistake whose error in timing was about 30 ns. A systematic relative difference of about 10 ns between the optimal timing for TOB with respect to TIB/TID and TEC is also visible. The statistical error of these measurements has been estimated to be about ± 1 ns.

The non-optimal sampling determines the loss in the signal performance of the various sub-detectors. On the right side of Fig. 16, the horizontal lines mark the offset corresponding to a loss of signal of 1%, 5%, and 10% respectively. The correction factor to compensate for the loss of signal is plotted for each run in Fig. 16. The anomalous week where a wrong latency was chosen, resulted in large correction factors: 10% for TOB and 35% for TIB/TID and TEC. Otherwise, the correction is less than 5% and this sets a scale for the expected accuracy of the absolute calibration. That is, in comparing results between sub-detectors or for the same sub-detector at different temperature conditions, this level of uncertainty is larger than, for example, the contributions from time-of-flight differences.

5.2 The signal-to-noise

The signal-to-noise quantity normalized to the sensor thickness (S_{ren}/N) should be largely independent of gain corrections and therefore allows a more accurate comparison of results from modules in the same layer or at different temperatures or from run to run. For this reason S_{ren}/N is an ideal parameter for measuring the stability of the Tracker during the Sector Test.

S_{ren} is the signal as defined in eq.3; N is the cluster noise, defined as $N = \sqrt{\sum_i N_i^2/n_{strips}}$ where N_i is the noise of the i -th strip of the cluster and n_{strips} is the number of strips of the cluster. It should be emphasized that if the noise is constant for all strips in the cluster, then the cluster noise is independent of the cluster size and equal to the strip noise. N_i is determined in each pedestal run and written to the offline database. It was not remeasured continuously during the cosmic data taking.

Results of S_{ren}/N performance at $T = -10^\circ\text{C}$ are shown in Fig. 17 for TIB, TOB and in Fig.18 for TID, TEC. The fit to the S_{ren}/N is based on a Landau function convoluted with a Gaussian, and therefore has four parameters. The range of the fit starts from a minimum value equal to the 10% of the peak, goes to a maximum equal to peak position plus three times the FWHM. The χ^2/ndf for the fit is excellent. For TEC and TID the statistics are lower than for TIB and TOB, since the rate of large angle cosmic tracks is much reduced with respect to vertical ones. All Tracker layers show a large S_{ren}/N , in all cases higher than 26.

A study of the stability of S_{ren}/N performance was done, examining measurements for every single run during long periods where the Tracker was running in stable conditions: the best periods are when the Tracker was running cold. Fig. 19 shows the results for TIB and TOB, for all the layers, versus the run number when Tracker was running at 0°C and -10°C : TIB and TOB show a very stable behavior with variations less than 0.3%. Similar results are obtained for TEC and TID, but the lower statistics per each run gives rise to a higher statistical error on the run by run measurement.

S_{ren}/N increases with decreasing temperature, as expected from the results on the temperature dependence of the noise. A more quantitative analysis of the temperature dependence was not possible since it requires an optimization of the APV25 parameters for each module geometry at each temperature.

After normalizing the signal to the sensor thickness, S_{ren}/N should be identical for identical modules, regardless to their position. Nevertheless, the segmentation of the silicon in microstrips, combined with the effect of the clustering algorithm, which uses thresholds to determine strip inclusion in a cluster, might introduce some charge loss. The fractional charge loss due to clustering threshold will be more significant when the charge is small. An analysis has been done based on the angle of incidence of the tracks, as charge tends to be shared among more strips at higher angles. Therefore the dependence on the track angle has been studied first with respect to the 3D

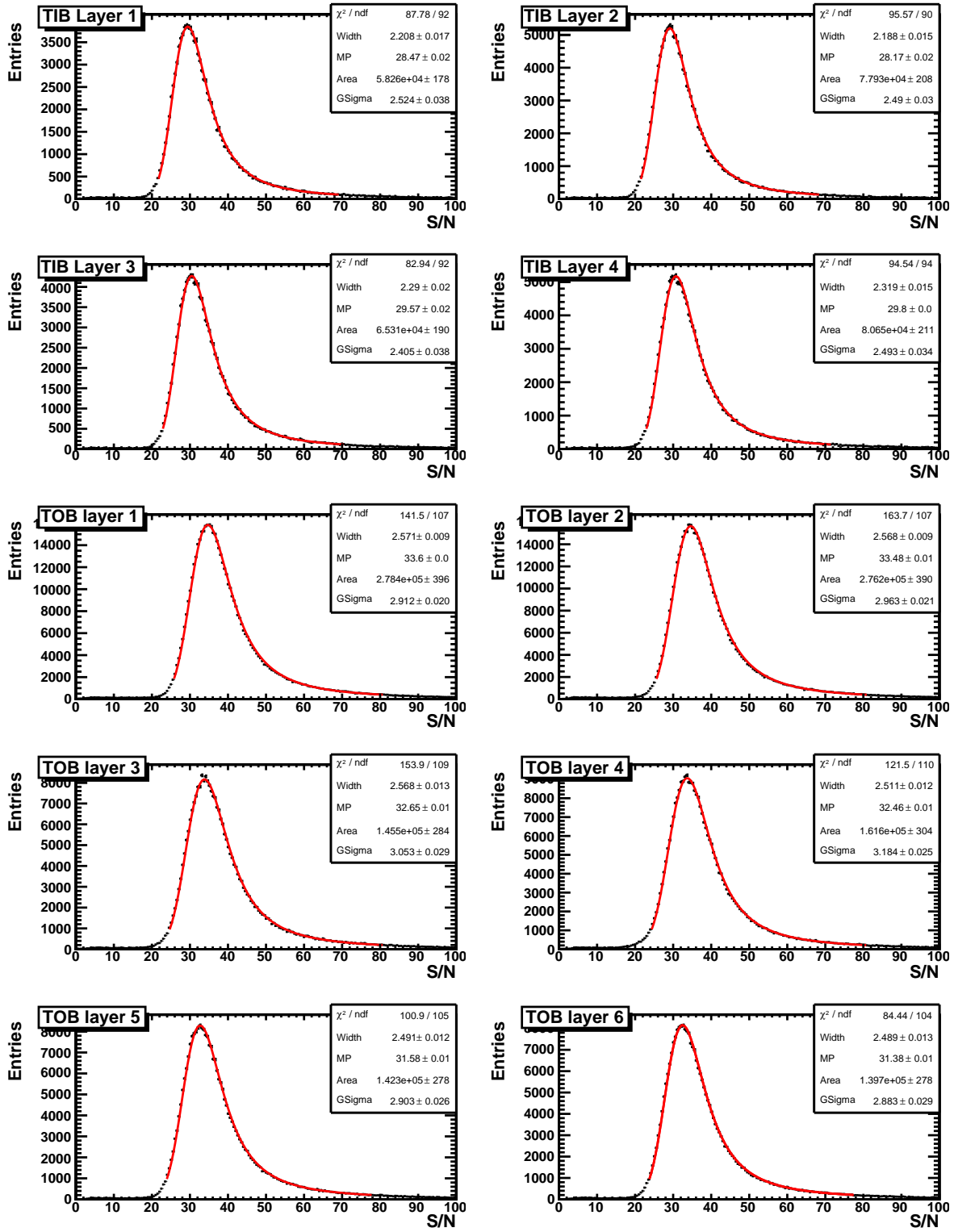


Figure 17: The signal-to-noise corrected for the track angle for TIB and TOB layers at $T = -10^\circ\text{C}$.

angle. In order to separate the effect of illuminating more strips from that of increasing the charge the study has been done for: the dependence on the XZ local angle for tracks perpendicular to the silicon strips (YZ local angle less than 6 degrees), referred as transverse tracks, where the sharing among strips is maximized; the dependence on the YZ local angle for tracks that come along the direction of the silicon strip (XZ local angle less than 6 degrees), referred as longitudinal tracks, where the sharing among strips is almost independent of the angle. These studies have been performed by looking at the dependence in S_{ren}/N on track path (K) within the silicon,

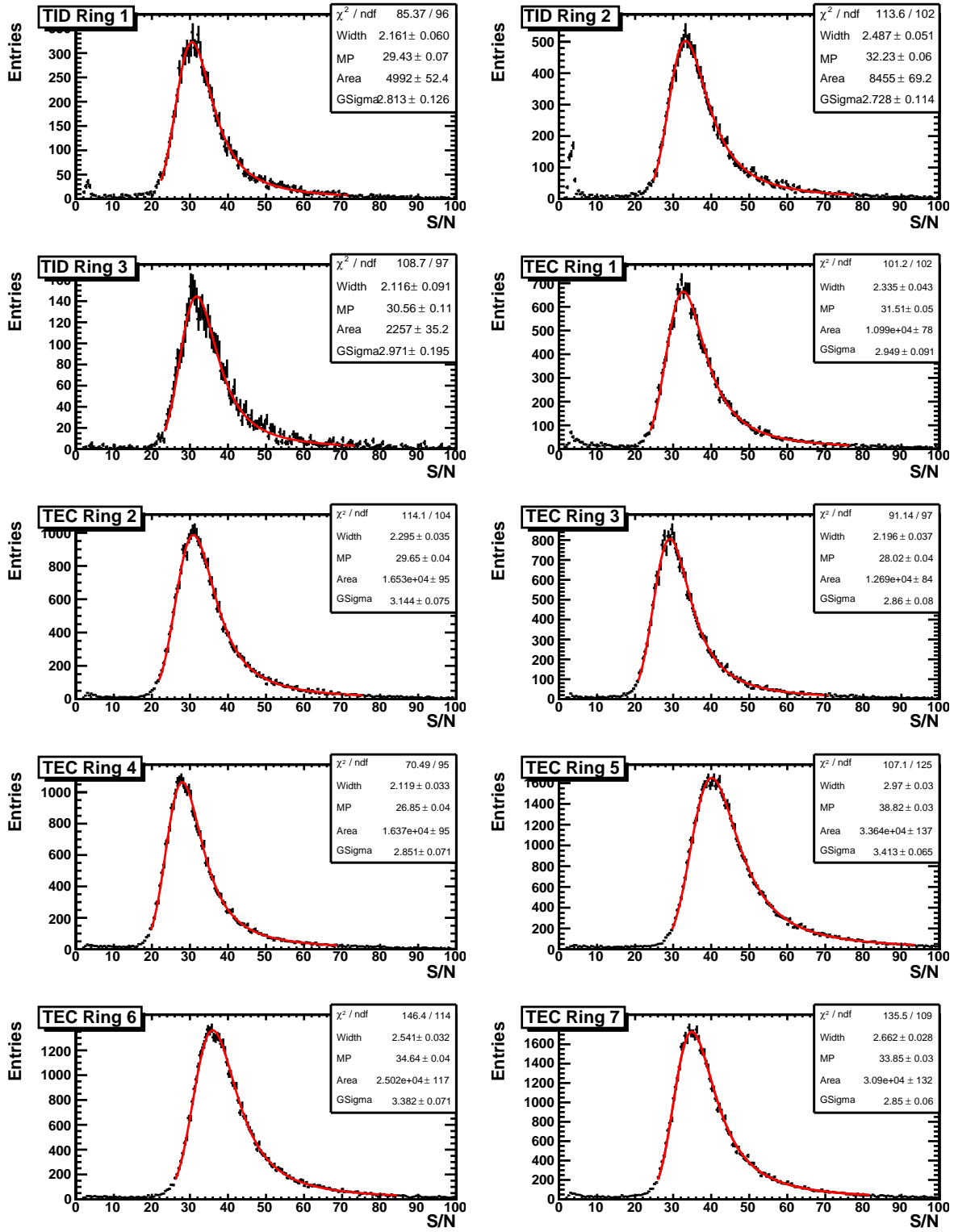


Figure 18: The signal-to-noise corrected for the track angle for TID and TEC rings at $T = -10 \text{ }^\circ\text{C}$

is expressed in units of silicon thickness. S_{ren}/N should be independent of K , see equation 3.

Results are shown in Fig. 20 for TIB and TOB: with black circles for the YZ angle and with open triangle for the XZ angle dependence. TEC and TID results have not been included since the variation of S_{ren}/N for the different rings is large and there is a correlation between K and the statistics for each ring.

It is clear in Figs. 20 that, for small K , there is a nearly 5% loss of S_{ren}/N (and presumably signal) for TIB. For

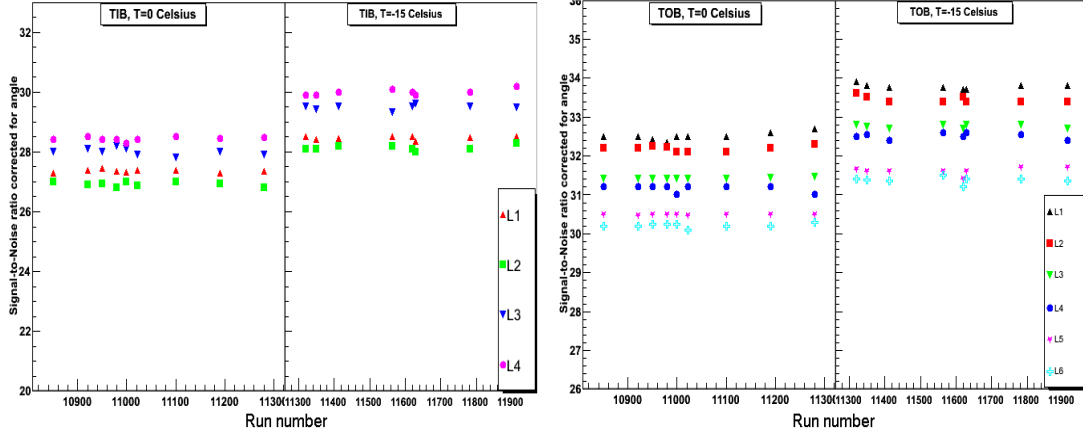


Figure 19: Signal over noise corrected for the track angle: from the left to the right for TIB and TOB.

longitudinal tracks most of the charge is concentrated in one strip, signal in neighbouring strips increases with K : once above the clustering threshold, they are included in the cluster and therefore almost all the charge delivered by the track is taken into account already for $K = 1.3$ where a sudden increase is visible. For transverse tracks the charge is shared among several strips and the charge loss at the edges of the cluster, will be less significant as K increases. For $K = 2$ the transverse and parallel tracks give the same signal-to-noise value.

For TOB a similar effect is seen, with a estimated loss of charge for small K of the order of nearly 6%: the charge of transverse tracks increases almost linearly with K and parallel tracks show a sudden increase at $K = 1.2$. Contrary to the TIB, for TOB the parallel tracks do not reach a constant value, but S_{ren}/N decreases starting for $K = 1.6$. This can be explained by the effect of departure from linearity of the APV25 for charges higher than 3 mip with gradual fall off beyond, that influences the tail of the Landau distribution for large charge release to single strips.

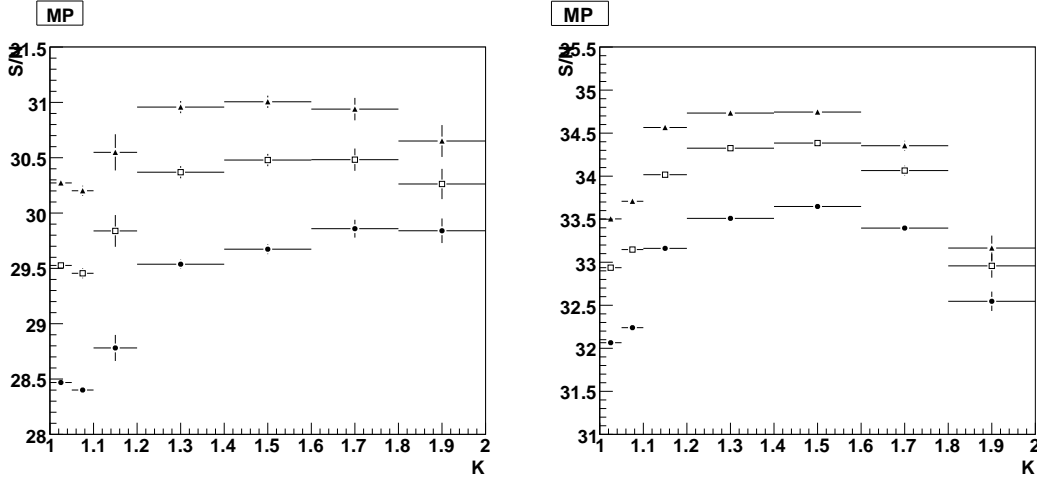


Figure 20: S_{ren}/N dependence on K for tracks perpendicular to the strip direction (open triangles) , i.e. the XZ local direction, and for tracks parallel to the strip direction (black circles) , i.e. the YZ local direction, for TIB and TOB.

5.3 Signal calibration

The correction for the electronic gain, see equation 1, can be used to improve the resolution on the signal performance. Fig 21 shows the uncorrected and the corrected signal. For all sub-detectors the calibration results in a decrease of the FWHM; it is clear that the electronic gain calibration improves the FWHM. In the case of the TEC, after the electronic calibration, two peaks are visible, which are the consequences of the use of thin and thick silicon sensors.

Having included this calibration it is interesting to check the level to which the absolute calibration is understood.

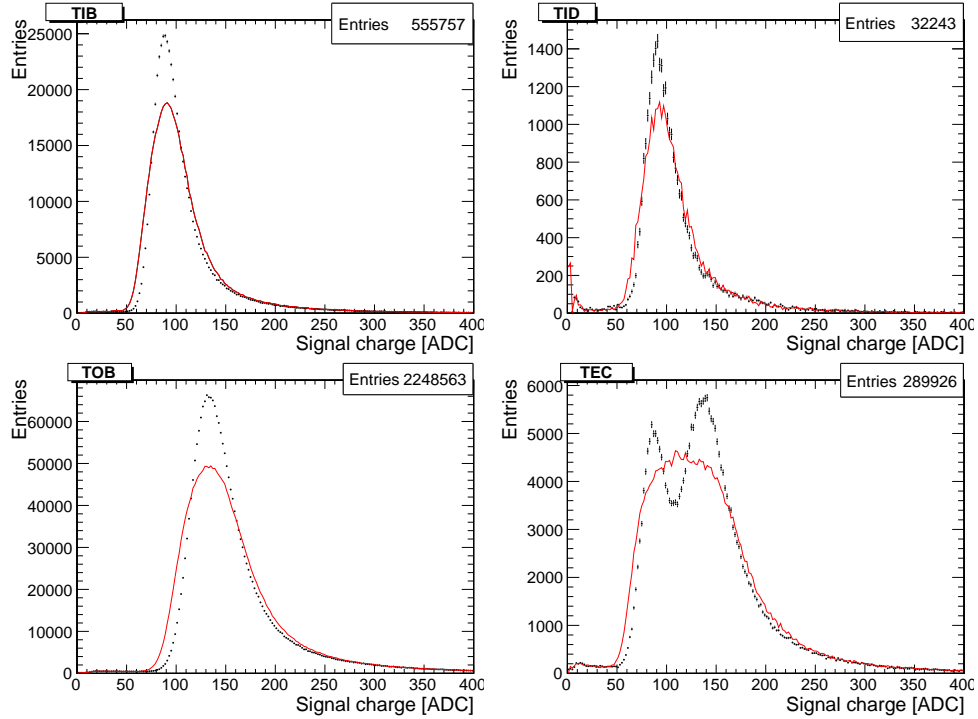


Figure 21: Signal corrected for the track angle (S_{ren}), in full curve without electronic gain calibration and in dots with it.

To do this, an analysis at the module level has been made, looking at the distribution of the most probable value of the signal, expressed in ADC counts, for the thin detectors (TIB and TEC rings 1 to 4), and for the thick detectors (TOB and TEC rings 5 to 7). Results are shown in Fig. 22 for the -10°C period.

Modules of the same sub-detector are well represented by Gaussian distributions with fairly large sigmas. These are at the level of 3.8% and 5.3% for TIB and TEC thin sensor modules; of 4.6% for TOB and TEC thick sensor modules. Therefore, single module signal performance can be understood to these levels of precision within the same sub-detector, to be compared with the spread of the tickmark height of about 13% before taking into account the electronic gain, see Fig 6. Further improvements in the evaluation of the electronic gain can come, for example, by taking into account the supply voltage for individual modules.

It should be noted that modules of the same geometry, but placed in different position, are differently illuminated by the cosmic rays and this varies S_{ren} as it can be seen in Figs.20. This introduces another level of complexity to this study.

Some lessons can also be learned by comparing the average results obtained by modules with silicon of the same thickness: for the TIB and thin sensor TEC modules, the average values are within 2.2%, while TOB and thick sensor TEC modules have average values that differ by 5%. It should be borne in mind that signal performance can be affected by changes in APV25 parameters. Typically, these are adjusted for reasons other than equalizing the peak amplitude of the output signal.

TEC has the interesting feature that all modules, both thin and thick, have been run with the same APV25 parameters. The ratio of the mean values of thick over thin sensor module signal is: $\frac{\langle \text{Signal}(\text{TEC}_{thick}) \rangle}{\langle \text{Signal}(\text{TEC}_{thin}) \rangle} = 1.614 \pm 0.008$, which is compatible with the ratio 1.62 of thicknesses of $470\ \mu\text{m}$ and $290\ \mu\text{m}$. This is not so precisely the case when TIB and TOB are compared.

In order to better understand the signal performance, this analysis has been performed at two different temperatures: 10°C and -10°C . The signal changes of 2-3% within a given layer for the 20 degrees change in temperature. It can be concluded that the conversion factor between ADC counts and electrons must be done at individual layer level for each temperature if a 5% level has to be reached. Further refinements to the calibration would require a module by module study based on track information.

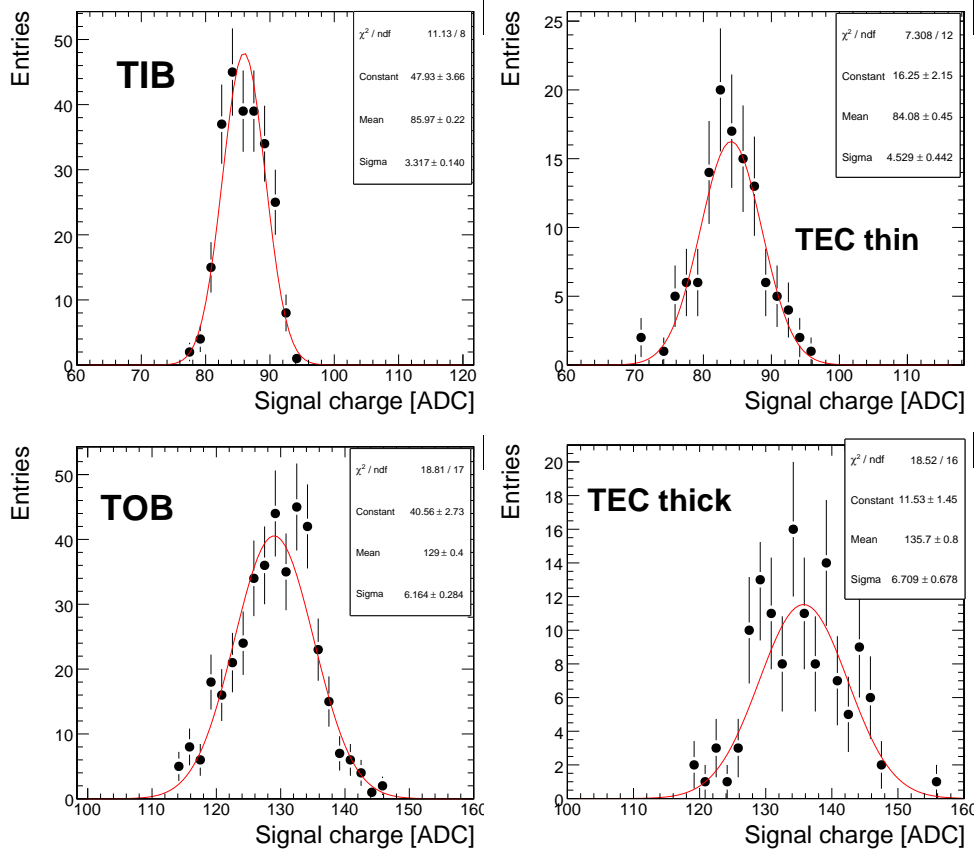


Figure 22: Distribution of signal (S_{ren}) most probable value, module per module for TIB (top left), TEC thin sensors (top right), TOB (bottom left), and TEC thick (bottom right).

5.4 Validation of Online Zero Suppression

The correct functioning of the FED clustering algorithm and its simulation was validated in the Sector Test through the study of cosmic data runs and special configuration runs.

Special runs were taken in which the data from a single TOB rod was optically split and sent simultaneously to two FEDs. One FED passed the data in VR mode, and the other applied ZS. Offline analysis of the output from each FED allowed a direct comparison of the FED ZS output with a simulation of the ZS algorithm applied to the VR data. Only small differences, consistent with gain variation between the two data paths, were observed.

Cosmic data was further used to validate the functionality of the FED. Several consecutive runs, one with ZS enabled and the second without ZS enabled, were taken and the data from these to check for global FED failures, to further validate the offline algorithm, and to study the effect of varying the thresholds.

The only significant difference, an excess at about 128 counts, is due to a small number of channels that had pedestals outside the range allowed by the FED.

5.5 Hit Occupancy

Occupancy for a given strip is defined as the fraction of events in which it registers a signal exceeding the threshold required to be “hit”. When LHC is running at high luminosity, the occupancy of the innermost strip layer (TIB L1) is estimated to be a few percent [1]. As described in the reconstruction section, seed strips and the cluster require a signal-to-noise value greater than 3 and 5 respectively. If strip noise is purely Gaussian then the probability of a statistical fluctuation to become a cluster is very low, less than $5 \cdot 10^{-5}$, and is therefore negligible. It is interesting to measure the subdetector occupancy during the Sector Test, by taking the mean value of the distribution of the probability of a strip to be in a cluster, that is, the strip occupancy distribution.

In order to separate the contribution coming from real tracks, the strip occupancy has been studied for clusters with S/N higher or lower than 20. Results are shown in Fig. 23 for TIB and TEC. Cosmic rays account for an

occupancy of $3.5 \cdot 10^{-6}$ (TIB) and $1.1 \cdot 10^{-6}$ (TEC) with no tails in the distribution. Clusters from statistical fluctuations accounts instead for occupancy of $2.5 \cdot 10^{-6}$ and $1.9 \cdot 10^{-6}$ and show much longer tails. It is apparent that there are strips that are more active than others, with strip occupancies up to 5% or larger.

It seems clear that the tails observed in some of the occupancy distributions are the result of active (“hot”) strips. These strips have not to be confused with the noisy strips described in Sect 4.3 since these “hot” strips are characterized by non-Gaussian fluctuations, above five times the noise value. The number of the “hot” strips with strip occupancy above 1% is below 0.05% and therefore does not significantly affect module occupancy. Similar results have been obtained for TOB and TID sub-detectors.

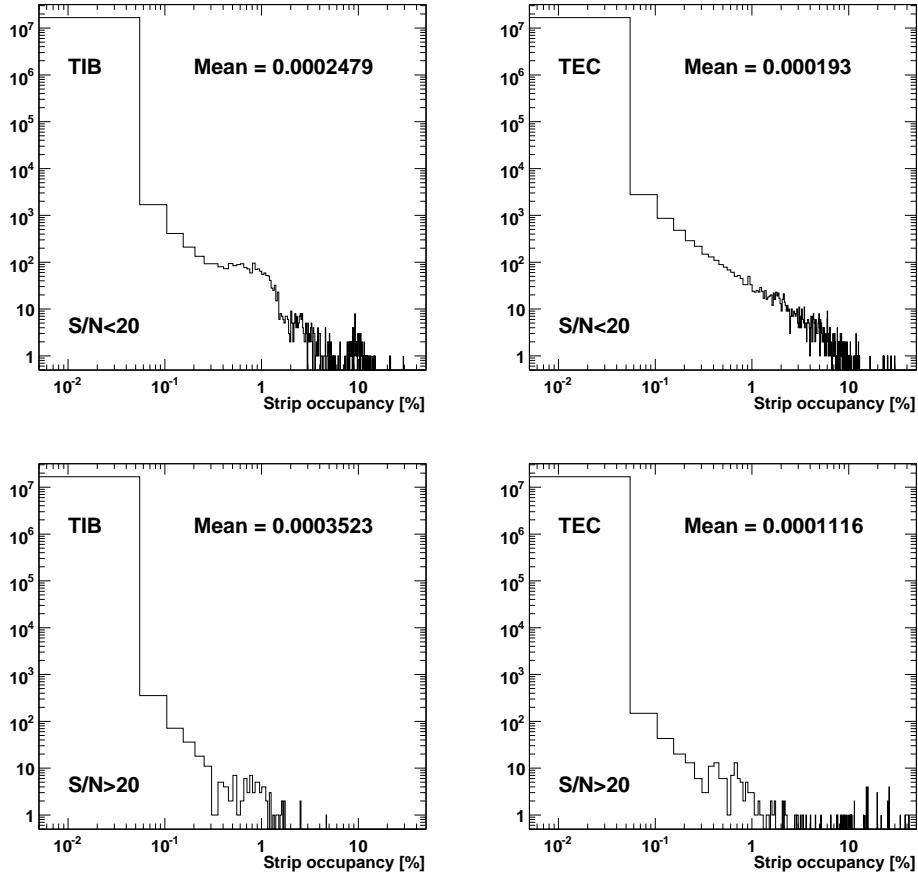


Figure 23: Distribution of strip occupancy for TIB and TEC: upper (lower) plots for S/N below (above) 20.

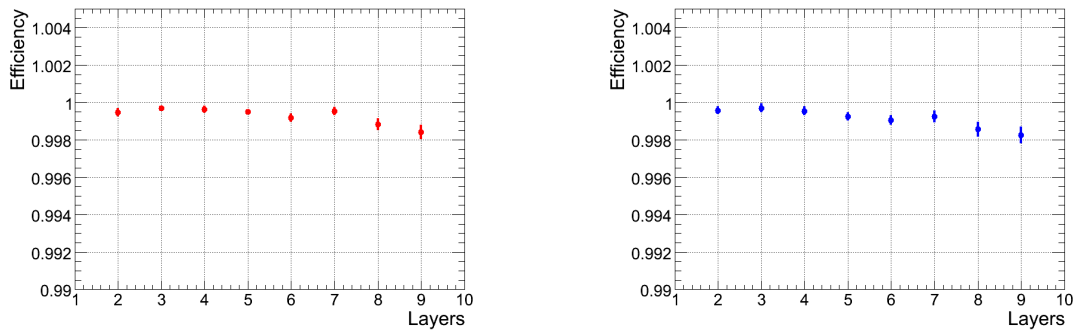


Figure 24: Summary of layer efficiency at room temperature (left) and at $T = -10 \text{ }^\circ\text{C}$ (right).

5.6 Hit Reconstruction Efficiency

The efficiency of a Tracker module to observe a hit when traversed by a particle, is one of the most important characteristics of the detector performance as this can be affected by losses in the silicon, electronic chain, or data acquisition and analysis. Efficiency has been measured by modifying the track reconstruction algorithm to skip the layer under study during the pattern recognition phase. A sample of high quality events was selected by requiring only one track reconstructed by the CTF algorithm, one hit in the first TIB layer, one hit in the two outermost TOB layers, and at least four reconstructed hits (of which at least three matched from stereo layers). Tracks were required to have no more than five lost hits during the pattern recognition phase and not more than three consecutive ones; finally an upper cut of 30° on θ_{3D} was applied to select tracks almost perpendicular to the modules.

In order to avoid genuine inefficiencies present at the edge of the sensor and in the bonded region between two sensors, additional cuts have been applied to restrict the regions in which efficiency is measured. With this event selection criteria and fiducial area restrictions, the efficiency exceeds 99.8% for all measured layers as is shown in Fig. 24. Additional details on the tracking and analysis procedures can be found in Ref. [4].

6 Simulation

Cosmic ray muons are simulated with the CMSCGEN generator[26] and the parameterizations of the energy dependence and incident angle are based on a generator developed for the L3+Cosmics experiment. The muon energy spectrum at the surface level TIF contains very soft muons and simulation is needed down to 0.2 GeV as this is the cutoff imposed by the 5 cm of lead. The uncertainties in the cosmic ray spectrum in this low energy range are very high and the CMSCGEN parameterizations do not permit an accurate simulation of muons below 2 GeV. For the TIF data simulation, the events with cosmic muons below 2 GeV are produced according to the energy spectrum measured by the CAPRICE[27] experiment that describes cosmic muons down to 0.3 GeV. The angular dependencies in this simulation are taken to be the same as for muons at 2 GeV. Using the CAPRICE energy spectrum, the remaining uncertainties at this low energy are largely due to solar modulation, angular correlations, latitude dependencies, altitude effects, the earth's magnetic field, and specifics of the building ceiling structure where the tests take place. However, this approximation of the energy spectrum seems satisfactory for Tracker commissioning purposes.

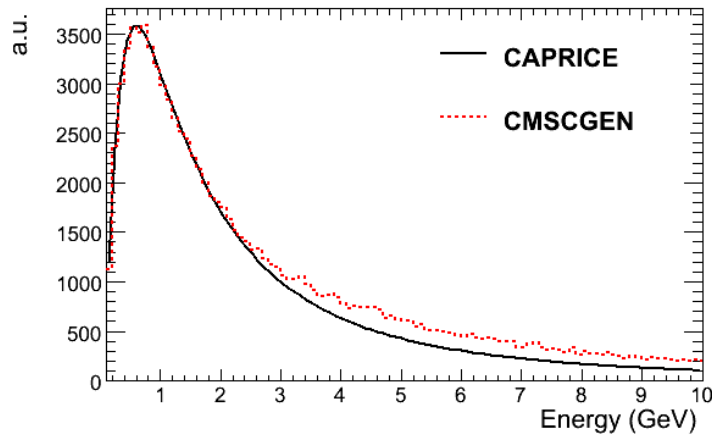


Figure 25: *The CMSCGEN cosmic muons energy spectrum. Below 2 GeV the events are reweighted according to the CAPRICE spectrum.*

Before the simulation stage, the generated cosmic muons are filtered in order to mimic the experimental trigger setup described in Section 2.6, where triggering was based on the coincidence of separated scintillation counter arrays. In order to simulate the effect of the trigger, the scintillators, three or four depending on the configuration, have been modeled as simple $1 \times 1 \text{ m}^2$ surfaces. Muons are initially extrapolated to the outer radius of the Tracker, the intersection points with the scintillator surfaces calculated, and the trigger logic applied. No materials other than those known to be present in the Tracker were taken into account in the simulation process. The ϕ and the η distributions of the simulated cosmic tracks for the two scintillator configurations are shown in Figure 26. The simulation includes the information of the Tracker region actually connected for the readout, this can be seen in Fig. 27 for the trigger Configuration TC.

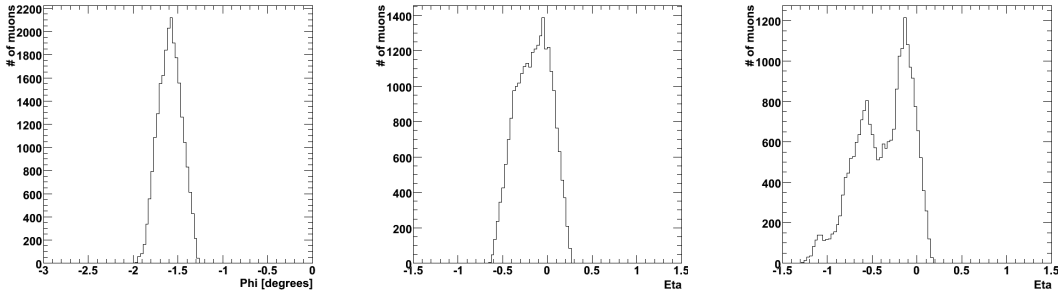


Figure 26: Cosmic muon track parameters: ϕ (left), η for scintillator *Conf(TA)*(middle) and *Conf(TC)*(right)

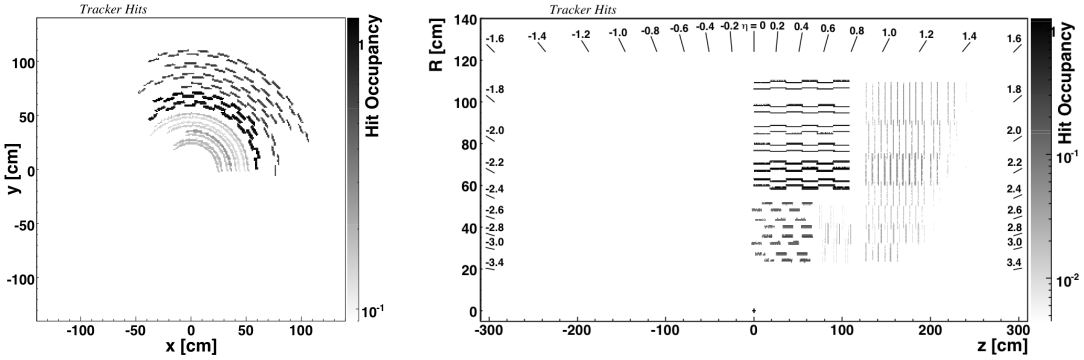


Figure 27: Hit distribution for the cosmic muons in the x - y (left) and y - z (right) plane in Configuration TC

Details of the signal and noise simulation implementation in the CMSSW software are described in [23] and will be quickly summarized here. GEANT4 propagates each track through the detector volume. The particle entrance and exit point is recorded for each sensitive layer, together with the deposited energy. During this step, cuts for δ -ray production are applied (120 keV for the strip Tracker sensitive volumes) tuned to optimize the timing of the simulation while minimizing the effects on the description of the the charge distribution. To digitize the signal collected by each channel, the charge is multiplied by a gain factor and rounded to the nearest integer, thus simulating ADC digitization. Signals exceeding the 8-bit ADC range are assigned the maximum allowed ADC value (256 ADC counts). The simulation of the response of the detector and the readout chain happens during this digitization phase. FED zero-suppression can also optionally be simulated. The code has been developed trying to balance the accuracy of the simulation, the timing performance, and the quality of the simulation in order to be able to reproduce position resolution, charge collection, detector efficiency and occupancy. The resulting one-dimensional charge distribution is mapped to the strip readout geometry and the fraction of charge collected by each readout channel is determined. After this step the simulated data can be treated by the reconstruction software in the same way as actual data.

7 Simulation Tuning

One of the main goals of the Tracker simulation is to be able to reproduce the detector response to real data from p-p collisions as accurately as possible. It is important to identify the quantities that are most sensitive to disagreements between real data and Monte Carlo and can have an impact on the performance of the simulation for physics analysis (for instance cluster position resolution, occupancy, track reconstruction efficiency and fake rate). The Sector Test was an opportunity to perform a first tuning of the simulation using cosmic muons, keeping in mind the limitations due to the fact that these muons do not have the same timing as collision particles and their momentum is unknown. However, the large statistics of the cosmic muons from the Sector test allow one to verify if the granularity available in the simulation parameters is adequate for achieving the tuning with real data. The quantities that received the most attention in this study relate to noise and signal clusters: noise is considered both at the individual channel level and for its effect on occupancy; whilst typical parameters in studying signal clusters include cluster width, absolute calibration (electrons to ADC counts), and charge sharing.

7.1 Signal and Noise

The noise simulation in the CMS Tracker, as explained in [23] is based on a parametrization of the equivalent noise charge (ENC) as a function of the strip length L and corresponds to:

$$ENC(Peak) = (38.8 \pm 2.1)e^{-} \text{cm}^{-1} \times L + (414 \pm 29)e^{-} \quad (5)$$

The noise measured with the data, as explained in Section 4, is compared with the parametrization in the simulation in Fig. 28. In the real data, effects such as temperature changes, can give rise to significant differences of the noise even for sensors of the same length. Other effects can also come into play (such as different APV settings) and a slight disagreement is present between the real and the simulated noise for the long sensors. One learns that an exact parametrization of the noise is not possible. To achieve a perfect simulation of it, the rms noise values used in the simulation, will have to be taken strip-by-strip from those measured with real data.

For the comparison with the simulation, it should be noted that both the noise and the signal generation is performed in terms of electrons and then converted in ADC counts using a factor that depends on the absolute calibration of the signal peak in data and MonteCarlo (for this analysis $e^{-}/ADC = 250$). It is important to emphasize the fact that an absolute calibration is meaningful only for a specific configuration of the APV parameters, running temperature etc. From signal studies presented earlier we can expect that an agreement around 5%-10% of the most probable value between data and simulation is satisfactory for our present purposes. The signal-to-noise of the Tracker is so large that such a difference in the simulation has nonetheless a negligible effect on macroscopic quantities related to physics, such as cluster or track reconstruction efficiency. This will not be true once the signal-to-noise drops due to irradiation. Hence, the tuning needs to be a continuous effort that follows the changes in the detector operation as a function of the integrated luminosity. The comparison for the Landau distribution obtained for clusters on tracks normalized to the angle of incidence on the sensor is shown in Fig. 29. The corresponding comparison for the signal-to-noise distributions is shown in Fig. 30. The bump that can be observed in the TOB signal and signal-to-noise distribution in the Monte Carlo is due to the fact that the Monte Carlo data are zero suppressed and saturate beyond 255 ADC counts, while the data used for this plot are in VR mode where there is no saturation effect until 1023 ADC counts. The effect is present also in the TIB and TEC detectors but is simply less visible in the plots. The discrepancy observed in the distribution of the signal charge in the case of the TEC detectors is due primarily to residual differences in the tracks impact angle in data and Monte Carlo and to the crude approximation of having in the simulation a single number to describe the interstrip capacitance coupling for the whole Tracker.

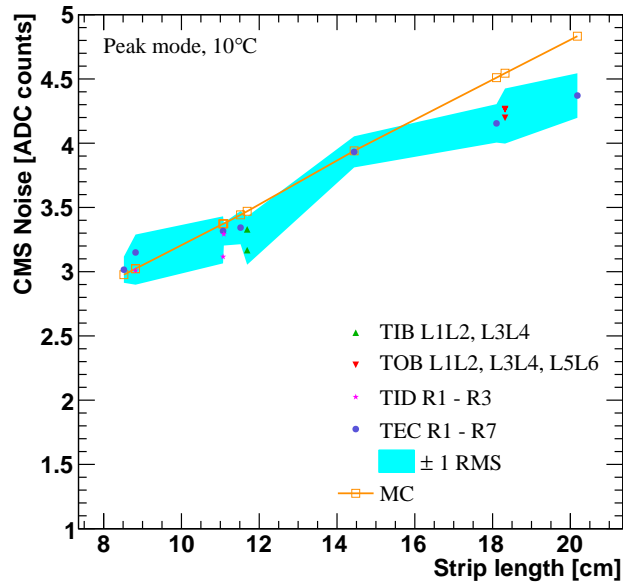


Figure 28: Measured noise in the various sub-detectors as a function of strip length compared with the Monte Carlo parameterization. The band corresponds to the spread of the mean noise in the layer.

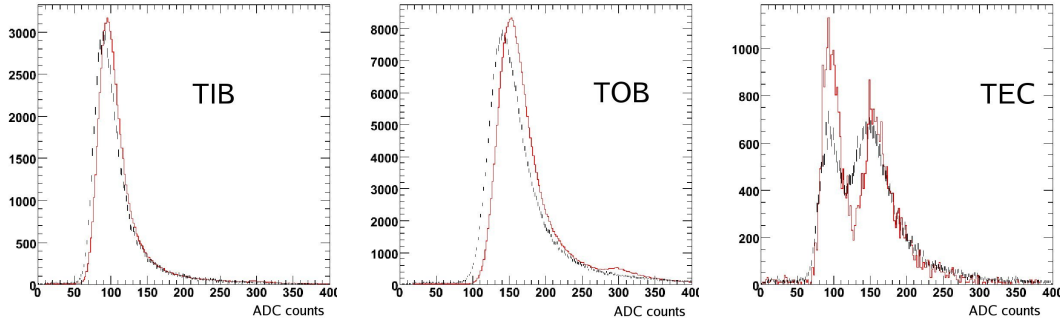


Figure 29: Signal distribution for clusters on tracks in data (dashed line) and Monte Carlo (solid line). From left to right: TIB, TOB and TEC

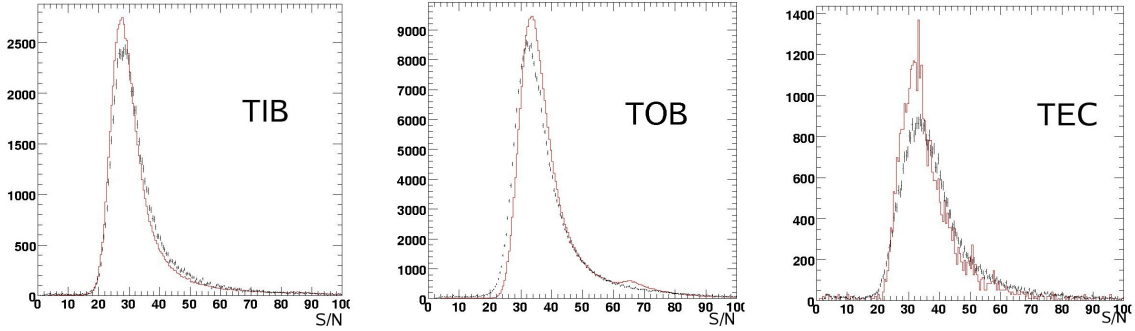


Figure 30: Signal to noise distribution for clusters on tracks in data (dashed line) and Monte Carlo (solid line). From left to right: TIB, TOB and TEC

7.2 Capacitive Coupling

The capacitive coupling is defined as the fraction of signal charge that is transferred from a signal strip (crossed by the minimum ionizing particle) to each of its neighbors. An important part of the simulation of the detector response is the simulation of the capacitive coupling of a strip with its nearest neighbour. The value is a configurable parameter of the simulation and at the time of this analysis, the default value used for the peak mode of operation was 7%, a preliminary value obtained from previous, low statistics, studies with cosmic muons [2]. In order to measure properly the capacitive coupling, one needs to disentangle it from other effects of charge sharing that are position dependent (such as diffusion, track inclination, Lorentz angle). A response function that can be used to extract the value of the capacitive coupling has been devised, that applies to the cases where the other charge sharing effects are minimized, that is for perpendicular tracks ($XZ\text{angle} \leq 0.1$ rad):

$$\eta(\text{symm}) = \frac{Q_{\text{left}} + Q_{\text{right}}}{2 \cdot Q_{\text{seed}}}$$

where Q_{seed} is the charge of the highest strip in the cluster and Q_{left} and Q_{right} the charges of its neighbors.

The measurement is performed on the Virgin Raw datasets that contain the information of the charge (positive or negative) for all the strips after pedestal subtraction. This allows one to define the eta functions also for single strip clusters using the charge of neighboring strips, even when below threshold. Clusters containing up to three strips have been considered for this analysis. This distribution is well modeled by a Gaussian plus a tail at positive value. The tail is due to the residual charge sharing and the width is due to the noise of the side strips. The η function is correlated in an analytical way to the value of the coupling:

$$CC = \frac{\eta}{1 + 2 \cdot \eta}$$

Fig. 31 shows the distribution of the “XZ” impact angle (defined in Section 5) between a track and a sensor in data and Monte Carlo (in Configuration TC). The difference in the angular distribution is due to the a shift in the position of the scintillator triggers between simulation and data. The distribution for the cluster width in data before and after the perpendicularity requirement is shown in Figure 32.

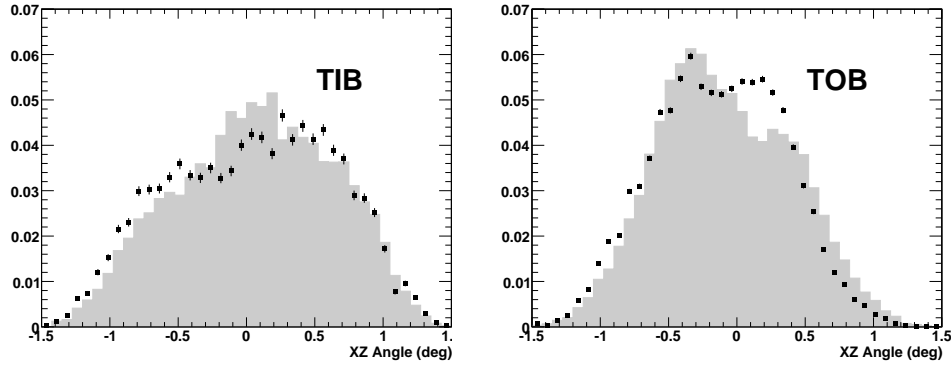


Figure 31: Local angle of incidence (XZ) for tracks on sensors in data (points) and MC (histogram) for TIB(left) and TOB(right)

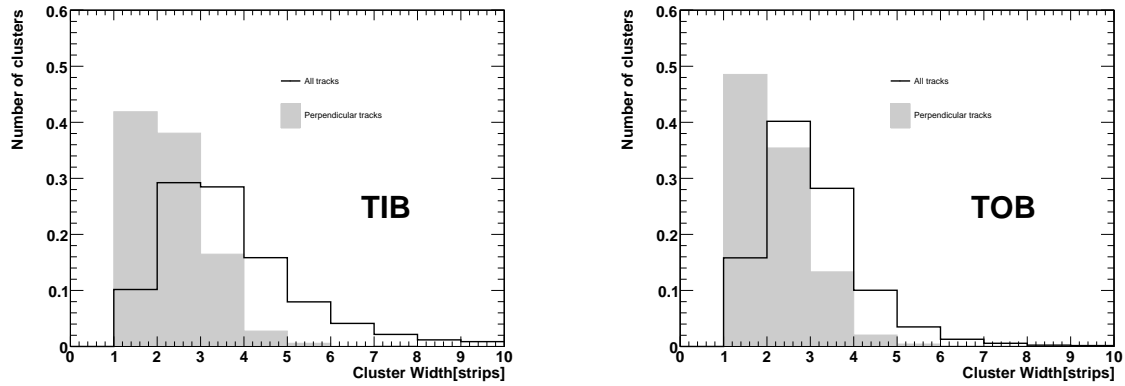


Figure 32: Cluster width for TIB(left) and TOB(right) hits for all tracks and perpendicular tracks

The distributions for the symmetric η function obtained from the Virgin Raw data are shown in Fig. 33 for the TIB and TOB respectively. From the position of the peak of the distribution of the coupling estimator a preferred value of 3.0% for the capacitive coupling is obtained. Given the strong dependence of the capacitive coupling on trigger timing shown by previous studies [29], and the non-standard timing configuration in the Sector Test, the results from the cosmic data do not allow to extract a precise measurement. Nonetheless, applying the best value of the capacitive coupling to the Monte Carlo the precision of the tuning can be seen comparing simulation to real data taken in ZS mode, see Fig. 34.

The cluster width is strongly affected by the change in the capacitive coupling constant. Figure 35 shows the excellent agreement for the cluster width for perpendicular tracks in the data, after the tuning of the capacitive coupling in the Monte Carlo.

7.3 Cluster width studies

In the presence of a magnetic field the diffusion path of charge carriers inside the bulk silicon will be influenced by the Lorentz force, which modifies the shape of the charge distribution of the clusters. The net effect is a shift in cluster position (relative to track intersection points) and a change of the cluster width. The shift and widening are largely due to charge drifting across cell boundaries, but the capacitive coupling between neighboring channels also has an influence on the final position and cluster width. In the case of the Sector Test, where there was no magnetic field, it is still interesting to evaluate the behavior of the cluster width as a function of the track incident angle perpendicular to the strip direction (angle XZ described in Fig.14 in Section 5) and compare the data and Monte Carlo distributions. Figure 36 shows the effect on cluster width of varying the impact angle when the capacitive coupling is changed from 7% to 3% in the simulation.

Since the value of the Lorentz angle might change as the silicon is irradiated a calibration strategy has been developed [28] which will determine and monitor its value from data and write it in the database, so that it can be retrieved by the offline analysis code, to correct cluster positions. TIF datasets have been used to validate and test this software with real data for the first time.

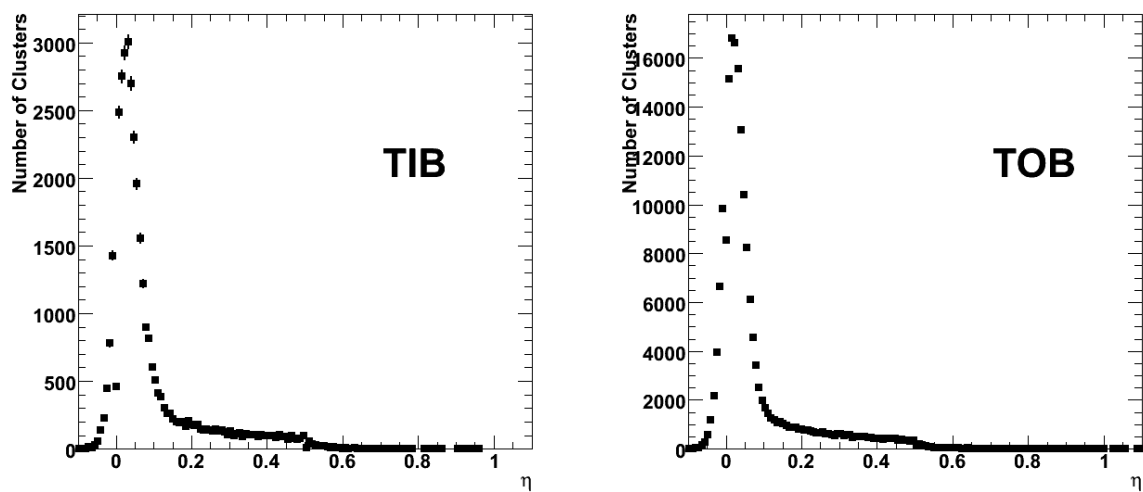


Figure 33: η function for TIB(left) and TOB(right) clusters. The data are from Virgin Raw runs where the information of the strips below the clustering threshold is available.

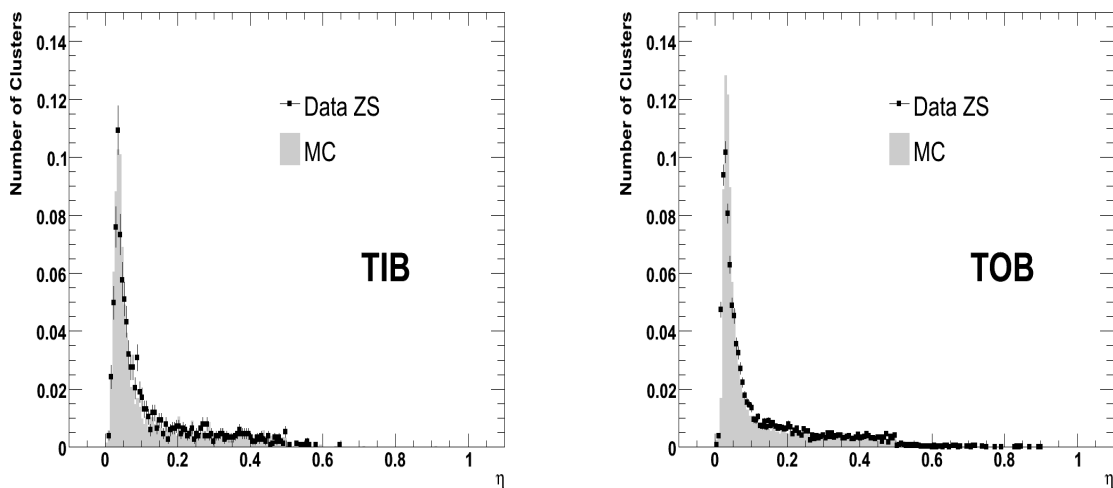


Figure 34: η function for TIB(left) and TOB(right) clusters. The data are from Zero Suppressed runs compared with Monte Carlo with 3% capacitive coupling.

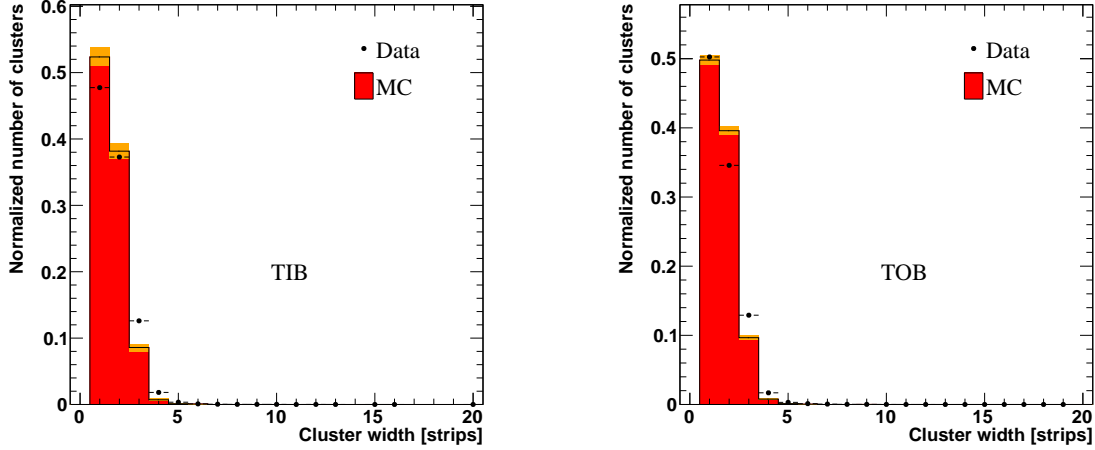


Figure 35: Cluster width for TIB(left) and TOB(right) hits on perpendicular tracks. The black points represent the data, the histogram is obtained from simulation with a 3% capacitive coupling where the gray band represents the statistical uncertainty.

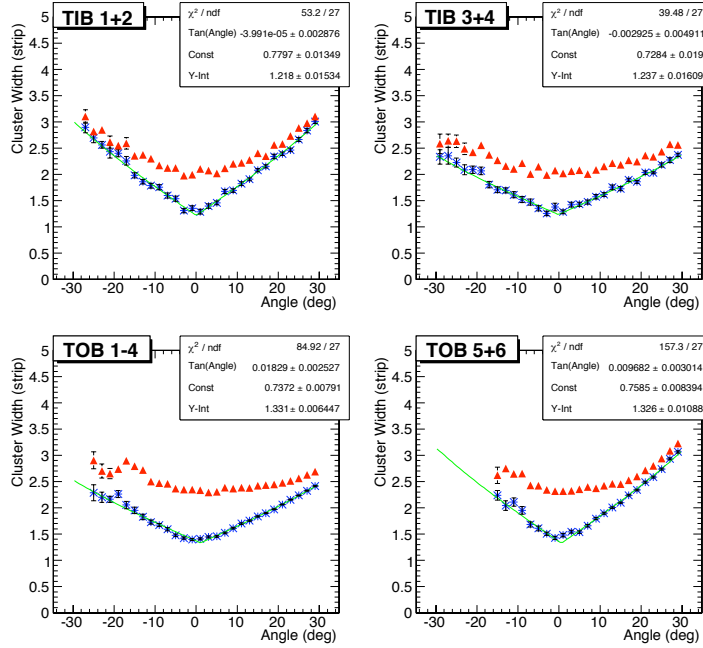


Figure 36: Cluster width versus θ_t for barrel layers on Monte Carlo simulated data using capacitive coupling of 7%(triangles) and 3% (crosses).

The average cluster width for tracks incident with an angle θ_t with respect to the detector normal is given by:

$$\langle \text{cluster width} \rangle = a + \left| \frac{t}{p} \cdot b \cdot (\tan \theta_t - \tan \Theta_L) \right|$$

where t is the detector thickness, p is the pitch, a and b are coefficients expressing the carrier diffusion and the electronic capacitive coupling between nearby channels, and Θ_L is the Lorentz angle. Therefore, plots of mean cluster width as a function of $\tan(\theta_t)$ are produced for each layer and the Lorentz angle is obtained fitting them with the function above. In this fit the parameters are: the estimate of the Lorentz angle ($\tan \Theta_L$), the slope normalized to the ratio of thickness over pitch (that should be constant), and the average cluster width at the minimum. Of course in the TIF setup there is no magnetic field and the Lorentz angle determination should return zero. The plots for each layer of the barrel detectors are shown in Figs. 37 and 38. The result from the data, grouped by layer with similar characteristics, has been overlaid by Monte Carlo result with a capacitive coupling

of 3% in Fig.39. The fitted Lorentz angles are consistent with zero as expected inside the statistical uncertainties, and with a disagreement of 2% at the most in some cases likely due to systematic misalignment effects. The comparison between distributions in real and simulated data indicates also that the granularity of the capacitive coupling constant in the simulation should be increased from the single value present now, to at the level of a parameter for each layer or even for each different type of module.

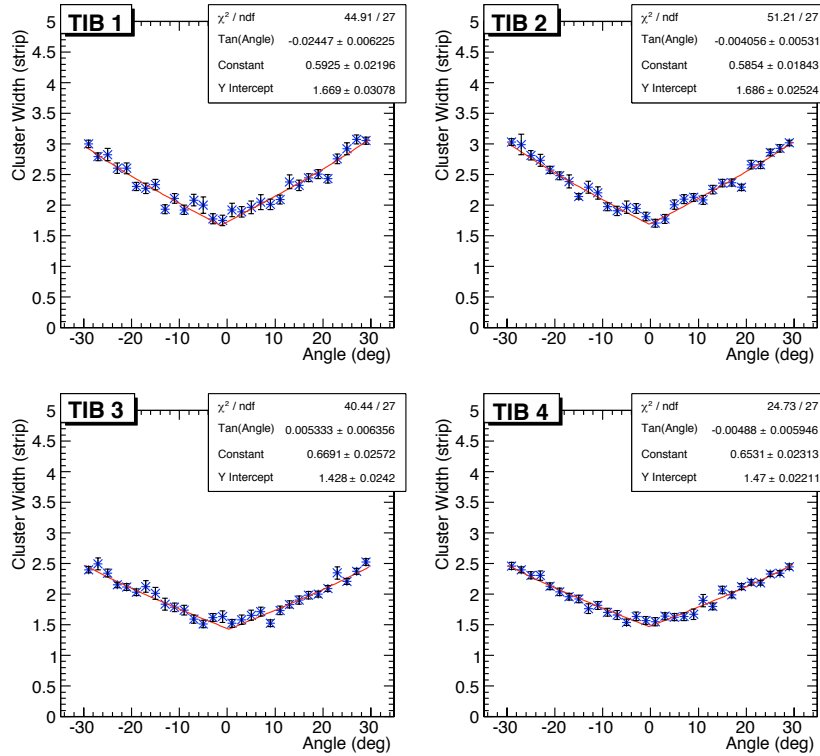


Figure 37: Cluster width versus θ_t for TIB layers.

8 Conclusions

The CMS Silicon Strip Tracker construction was completed in March 2007 at the CERN Tracker Integration Facility.

During the Sector Test, which spanned a period of about four months, the Tracker was operated in a stable and continuous manner for periods up to few consecutive weeks. Safe operations were established while running in different configurations and over a wide range of temperatures, from 15°C to -15°C . The 4.5 million cosmic rays events collected demonstrate the successful operation of the entire electronic chain of data acquisition system and the commissioning of such a large fraction of the detector for the first time.

The results of the data analyses here described show the excellent detector performance. The behavior of the noise and signal-to-noise has been very stable for all sub-detectors, better than 0.6%. In particular, the signal-to-noise in peak mode is larger than 26 for all layers or rings and the hit reconstruction efficiency is above 99.8%. The fraction of bad strips is 0.2% and of bad components is 0.6%.

Comparing the data with the expectations from the simulation for signal, noise, cluster width and capacitive coupling has allowed a preliminary tuning of the simulation input parameters. The agreement between data and simulation is at a level to allow large production of datasets to be used for early physics studies to be carried out with the first collision data in 2008.

The sector test has been a very important milestone achieved by the Silicon Strip Tracker and can be considered one of the best reference points for operating the full detector and understand its performance even after completion of the CMS experiment in 2008.

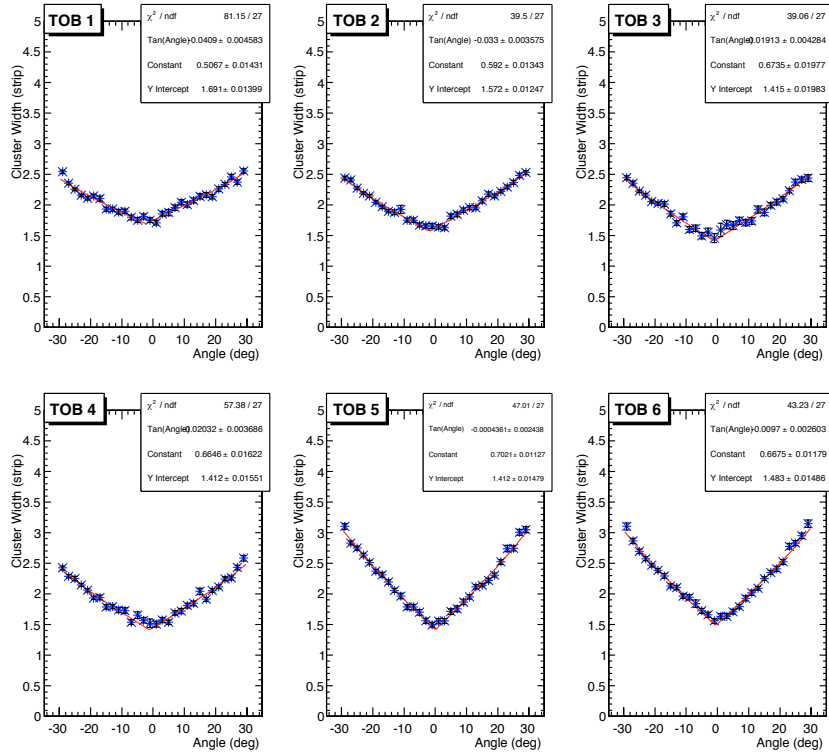


Figure 38: Cluster width versus θ_t for TOB layers.

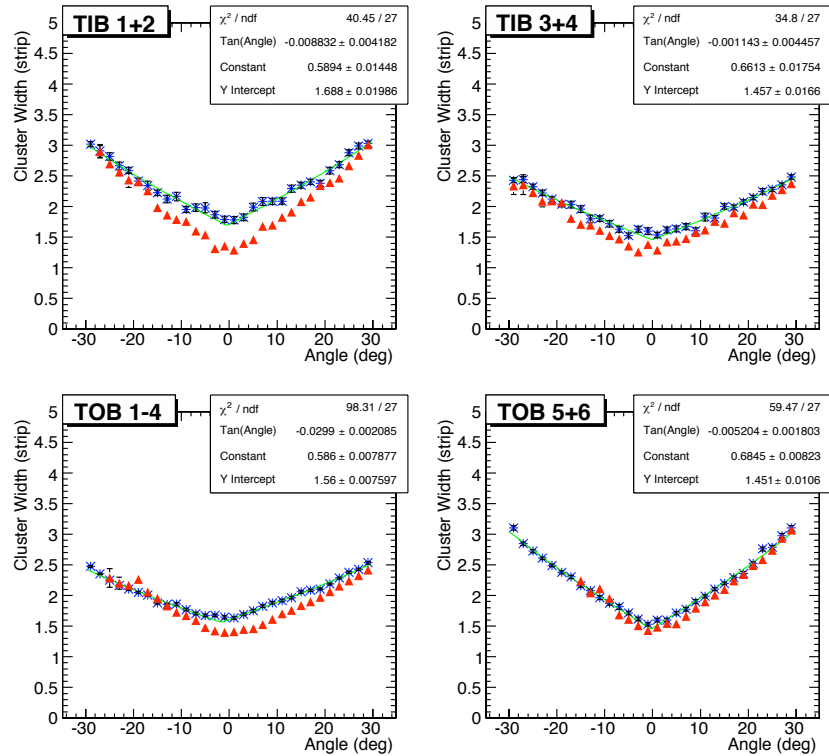


Figure 39: Cluster width versus θ_t for barrel layers on real data (crosses) compared with Monte Carlo (triangles) using capacitive coupling of 3%.

Acknowledgments

We thank the administrative staff at CERN and other Tracker Institutes. This work was supported by: the Austrian Federal Ministry of Science and Research; the Belgium Fonds de la Recherche Scientifique and Fonds voor Wetenschappelijk Onderzoek; the Academy of Finland and Helsinki Institute of Physics; the Institut National de Physique Nucléaire et de Physique des Particules / CNRS, France; the Bundesministerium für Bildung und Forschung, Germany; the Istituto Nazionale di Fisica Nucleare, Italy; the Swiss Funding Agencies; the Science and Technology Facilities Council, UK; the US Department of Energy, and National Science Foundation. Individuals have received support from the Marie-Curie IEF program (European Union) and the A.P. Sloan Foundation.

References

- [1] The CMS Collaboration, *CMS: The Tracker Project Technical Design Report*, **CERN-LHCC-98-06** (1998)
Addendum to CMS Tracker TDR, **CERN-LHCC-2000-016** (2000)
- [2] W.Adam et al., CMS Tracker Collaboration, *Tracker Operation and Performance at the Magnetic Test and Cosmic Challenge*, CMS Note 2007/029.
- [3] CERN Courier 48 (2008) 22
- [4] *Track Reconstruction with Cosmic Rays Data at the Tracker Integration Facility*, CMS-CR 2008/006
- [5] *CMS Tracker Alignment at the Tracker Integration Facility*, CMS-CR 2007/081.
- [6] M.J. French et al., *Design and results from the APV25, a deep sub-micron CMOS front-end chip for the CMS tracker*, Nucl. Inst. and Methods **A466** 359–365 (2001).
- [7] M. Raymond et al., *Final Results from the APV25 Production Wafer Testing*, 11th Workshop on Electronics for LHC and Future Experiments, Heidelberg, Germany (2005) 453–457.
- [8] M.-T. Brunetti, B. Checucci, V. Postolache, D. Ricci, *Electrical Qualification of the Pre-production of Analogue Opto-Hybrid Circuits for the CMS Tracker Inner Barrel and Inner Disks*, CMS Note **2003/027**
- [9] C. Foudas et al., *The CMS Tracker Readout Front End Driver*, IEEE Trans. Nucl. Sci. **52** 2836–2840 (2005).
- [10] G. Iles et al., *Performance of the CMS silicon tracker front-end driver*, 10th Workshop on Electronics for LHC and Future Experiments, Boston, USA (2004) 222–226.
- [11] K. Kloukinas et al., *FEC-CCS: A common front-end controller card for the CMS detector electronics*, 12th Workshop on Electronics For LHC and Future Experiments, Spain (2006) 179–184.
- [12] J. Troska et al., *Optical readout and control systems for the CMS tracker*, IEEE Trans. Nucl. Sci. **50** 1067–1072 (2003).
- [13] E. Noah et al., *Qualification of the CMS Tracker Control Link Digital Optohybrid*, 10th Workshop on Electronics for LHC and Future Experiments, Boston, USA (2004) 169–173.
- [14] C. Paillard, C. Ljuslin, A. Marchioro, *The CCU25 : a network oriented communication and control unit integrated circuit in a 0.25 μm CMOS technology*, 8th Workshop on Electronics for LHC Experiments, Colmar, France (2002) 174–178.
- [15] P. Moreira, A. Marchioro, P. Placidi, *CMS Tracker PLL Reference Manual*, CERN Report **cer-002725460** (2000).
- [16] G. Magazzù, A. Marchioro, P. Moreira, *The detector control unit : an ASIC for the monitoring of the CMS silicon tracker*, IEEE Trans. Nucl. Sci. **51** 1333–1336 (2004).
- [17] J. Gutleber, L. Orsini, *Software Architecture for Processing Cluster Based on I2O*, Cluster Computing **5** 55–64 (2002).
- [18] R. Bainbridge et al., *Commissioning and Calibrating the CMS Silicon Strip Tracker*, 12th Workshop on Electronics For LHC and Future Experiments, Valencia (2006) 419–423.

- [19] S. Paoletti et al., *The Powering Scheme of the CMS Silicon Strip Tracker*, Proceeding of the 10th Workshop on Electronics for LHC and future Experiments, Boston, USA (2004).
- [20] Frank Hartmann for the CMS Tracker Control Safety Group, *The CMS Tracker Control & Safety System*, Proceedings Vienna Conference on Instrumentation 2007. Submitted to NIM.
- [21] M. Frey for the CMS Tracker Collaboration, *The CMS-tracker detector control system.*, Prepared for 9th ICATPP Conference on Astroparticle, Particle, Space Physics, Detectors and Medical Physics Applications, Villa Erba, Como, Italy, 17-21 Oct 2005. Published in Como 2005, Astroparticle, Particle and Space Physics, Detectors and Medical Physics Applications, Oct (2005) 1067–1071.
- [22] ETM professional control GmbH, www.etm.at
- [23] The CMS Collaboration, *Detector Performance and Software Physics Technical Design Report*, Vol. 1, CERN/LHCC 2006/001, CMSTDR 8.1
- [24] C. Leonidopoulos, *Physics and Data Quality Monitoring at CMS*, Proceedings of CHEP06, Mumbai, India (2006).
- [25] C. Delaere, L. Mirabito, *Timing of the CMS tracker. Study of module properties.*, CMS Note 2007/027
- [26] P. Biallass, T. Hebbeker, *Improved parameterization of the Cosmic Muon Flux for the Generator CMSCGEN*, CMS Note 2007/033
- [27] M. Boezio et al., (CAPRICE Collaboration) Phys. Rev. D **67**, 072003 (2003)
- [28] Ciulli V., D'Alessandro R., Frosali S., Genta C. *Determination of the Lorentz Angle in Microstrip Silicon Detectors with Cosmic Muons* CMS Note 2008/006
- [29] *Studies for the commissioning of the CERN CMS Silicon Strip Tracker* C. Bloch, Ph.D. Thesis, Technische Universitat Wien, Fakultat fur Technische Physik, December 17 2007